

Halo Phenomenon in Medium-Mass Nuclei.

I. New Analysis Method and First Applications

V. Rotival*

DPTA/Service de Physique Nucléaire - CEA/DAM Île-de-France - BP12 - 91680 Bruyères-le-Châtel, France and
National Superconducting Cyclotron Laboratory, 1 Cyclotron Laboratory, East-Lansing, MI 48824, USA

T. Duguet†

National Superconducting Cyclotron Laboratory and
Department of Physics and Astronomy, Michigan State University, East Lansing, MI 48824, USA
(Dated: February 9, 2020)

The formation of haloes in medium-mass nuclei is investigated using a new analysis method, as available ones are proven to be incomplete/inaccurate. A decomposition of the intrinsic wave function of the N -body system in terms of overlap functions allows a model-independent analysis of the asymptotic properties of the intrinsic one-body density. The existence of a spatially decorrelated region in the nuclear density profile is related to the existence of typical energy scales in the excitation spectrum of the $(N - 1)$ -body system. Several model-independent criteria, taking the density as the only input, are introduced. The latter criteria allow a precise quantification of halo systems in terms of the average number of participating nucleons and of their impact on the nuclear extension. Those new "halo factors" are validated through simulations and used in connection with self-consistent mean-field methods. Performing spherical Hartree-Fock-Bogolyubov (HFB) calculations with state of the art Skyrme and pairing functionals, a collective halo is predicted in drip-line Cr isotopes, whereas no significant effect is seen in Sn isotopes.

PACS numbers: 21.10.Gv, 21.10.Pc, 21.60.-n, 21.60.Jz, 27.50.+e, 27.60.+j, 27.60.+q
Keywords: halo; mean-field; medium-mass nuclei

I. INTRODUCTION

The study of light nuclei at the limit of stability has been possible in the last two decades thanks to the first generation of radioactive ion beam facilities. One of the interesting phenomena observed is the formation of nuclear haloes. In such systems, either the proton or the neutron density displays an unusually extended tail due to the presence of weakly bound nucleons [1]. Since the first experimental observation of such an exotic structure in ^{11}Li [2, 3], other light neutron halo systems have been identified, for instance ^6He [4], ^{11}Be [5, 6, 7], ^{14}Be [5, 8], ^{17}B [5] or ^{19}C [9, 10]. On the proton-rich side, theoretical works demonstrated the possible existence of halo structures in spite of the Coulomb barrier [11], as was seen experimentally for ^8B [12, 13, 14, 15] and ^{17}Ne [16, 17]. Haloes in excited states have been observed for ^{17}F [18, 19], ^{12}B [20] or ^{13}B [21], and several others were predicted [22].

Theoretical descriptions of light halo systems are well under control. They rely on a cluster vision where one (^{11}Be , ^{19}C) or two (^{11}Li , $^6\text{He}\dots$) loosely bound nucleons define a low-density region surrounding a core. Assuming that core and halo degrees of freedom can be decoupled, essentially exact solutions of the simplified many-body problem can be obtained by solving the

Schrödinger equation for two-body systems [23, 24], or Faddeev equations for three-body ones [4, 23, 25, 26]. However, the boundary between halo and non-halo nuclei is blurred by the presence of core excitations. Indeed, inert decoupling of the loosely bound nucleons from the core is only an approximation. Nevertheless it has been assessed that halo systems arise when [27, 28] : (i) the probability of nucleons to be in the forbidden region outside the classical turning point is greater than 50% (ii) the cluster structure is dominant and accounts for at least 50% of the configuration. Such conditions have been thoroughly studied [29, 30] and found to be fulfilled when (i) the separation energy of the nucleus is very small, in order of $2 \text{ MeV}/A^{2/3}$ (ii) the loosely bound nucleons occupy low angular momentum states ($l = 0$ or $l = 1$) for two-body clusters, or low hyperangular momentum states ($K = 0$ or $K = 1$) for three-body ones, in order to limit the effect of the centrifugal barrier preventing the nucleons from spreading out [31] (iii) the charge of the core does not exceed $Z \approx 10$ for proton haloes.

When going to heavier nuclei, few-body techniques face theoretical and computational limits because of the large number of degrees of freedom involved. Energy Density Functional (EDF) [32, 33, 34] approaches based on the self-consistent Hartree-Fock-Bogolyubov (HFB) method become appropriate [35, 36]. Energy functionals, either non-relativistic (Skyrme [37, 38] or Gogny [39]) or relativistic [40, 41, 42, 43, 44], constitute the only phenomenological input to the method. Many questions still

*Electronic address: vincent.rotival@polytechnique.edu

†Electronic address: duguet@nscl.msu.edu

need to be addressed in order to formulate HFB-based calculations of self-bound systems within a truly functional approach [45, 46]. Phenomenological functionals have now reached an accuracy suitable for comparison of various observables with experimental data over the known part of the nuclear chart [47, 48, 49, 50]. However, properties of current density functionals are not yet under control in extreme conditions, where low-density configurations, isospin or surface effects come strongly into play. Thus, the capacity of existing functionals to predict properties of exotic nuclei, such as their limits of stability, remains rather weak [51]. In that respect, the input from the coming generation of radioactive beam facilities (FAIR, RIBF, REX-ISOLDE, SPIRAL2...) will help to further constrain models and to design a Universal Energy Density Functional (UNEDF).

Halo structures can play a significant role in that request, as they emphasize low-density configurations and surface/finite-size effects. Their study in medium-mass nuclei should provide important information regarding isovector-density dependencies and gradient/finite-size corrections in the energy functional. The pairing strength in low density regimes and the evolution of shell structures at the limit of stability might also be further constrained. However, two questions arise as we discuss potential medium-mass haloes. Indeed, medium-mass nuclei are (i) large enough that the cluster picture at play in light nuclei needs to be revisited, in such a way that our understanding of the halo phenomenon might change significantly (ii) light enough that explicit correlations associated with symmetry restorations and vibrational motions are important and may impact halo properties. This could call for extended EDF methods based on, for instance, the Projected Generator Coordinate Method [52, 53, 54].

The first part of the present work is dedicated to a new method to identify and characterize halo-type structures in medium-mass nuclei. A second article [55] will be devoted to a large scale analysis of halo properties in medium-mass nuclei using self-consistent HFB methods and the tools introduced here. In particular, key issues related to the impact of pairing correlations on haloes will be addressed.

In both papers, we focus on spherical even-even nuclei. Further extensions of the method to odd and deformed systems can be envisioned. The charge restriction for proton haloes identified in light nuclei is such that we do not expect proton haloes in medium-mass systems. Thus the largest part of the present work focuses on exotic structures at the neutron drip-line.

The present paper is organized as follows : SEC. II provides a quick overview of existing theoretical works and methods used to characterize skins and haloes within EDF approaches, whose basic aspects are briefly recalled. In particular, the limitations of the Helm model are discussed. A new method to properly characterize weakly-bound systems in a model-independent fashion is introduced in SEC. III. We validate the method using toy

models before applying it to the results obtained from self-consistent spherical HFB codes for Cr and Sn isotopes in SEC. IV. The latter section is also devoted to a critical discussion of our results.

II. BASIC FEATURES OF HALO SYSTEMS IN MEAN-FIELD APPROACHES

We present here an overview of existing works dedicated to identifying halo signatures in N -body systems. The purpose is to introduce the essential features which will turn out to be useful later. Our goal is also to demonstrate the limitations of existing analysis tools.

As usually done, we start in SEC. II A from an independent particle picture, and discuss how halo systems arise in the Hartree-Fock (HF) framework. Then, pairing correlations are added through the Hartree-Fock-Bogolyubov (HFB) method. The basic features of the latter method are recalled and the role of pairing is discussed in SEC. II B. Results from HFB calculations of chromium and tin isotopic chains are briefly reviewed in SEC. II C to introduce currently used halo observables. Finally, the Helm model is applied to those two isotopic chains and its limitations are discussed in SEC. II D.

A. Importance of low angular momentum orbits

At the Hartree-Fock level, nucleons evolve independently in their self-created mean-field V . Following REF. [56] for spherical one-neutron haloes (extended to deformed systems in REF. [57]), one starts by analyzing the asymptotic properties of bound neutron single-particle wave functions ϕ_i . They are solutions of the radial one-body Schrödinger equation⁽¹⁾ :

$$\left(\frac{d^2}{dr^2} + \frac{2}{r} \frac{d}{dr} - \frac{l(l+1)}{r^2} - \frac{2m}{\hbar^2} V(r) - \kappa_i^2 \right) \bar{\phi}_i(r) = 0, \quad (1)$$

where r is the radial coordinate, l the orbital angular momentum, and m the neutron mass. The decay constant

$\kappa_i = \sqrt{\frac{-2m\epsilon_i}{\hbar^2}}$ is related to the neutron single-particle energy $\epsilon_i < 0$ ⁽²⁾. Beyond an arbitrary large distance R , the mean-field potential vanishes because of the short-range nature of the nuclear interaction, and the asymptotic radial part of the wave function $\bar{\phi}_i^\infty$ satisfies the free Schrödinger equation. It reads as :

$$\bar{\phi}_i^\infty(r) = B_i h_l(i \kappa_i r), \quad (2)$$

¹ In the following, the radial part of a wave function $f(\vec{r})$ is noted $\bar{f}(r)$

² To make a connection with SEC. III, ϵ_0 will denote the single-particle energy of the least bound orbital : $\epsilon_0 > \epsilon_1 > \epsilon_2 \dots$

where B_i stands for the Asymptotic Normalization Coefficient (ANC) and $h_l(z) \equiv j_l(z) + i n_l(z)$ for the spherical Hankel functions, j_l and n_l being spherical Bessel and Von Neumann functions, respectively. Spherical Hankel functions read as :

$$h_l(i \kappa_i r) = i^l \frac{e^{-\kappa_i r}}{(\kappa_i r)} \sum_{k=0}^l \frac{1}{(2\kappa_i r)^k} \frac{(l+k)!}{k!(l-k)!}. \quad (3)$$

The associated one-body density $\rho(r)$ behaves asymptotically as $\frac{e^{-2\kappa_0 r}}{(\kappa_0 r)^2}$, where the decay constant κ_0 is related to the single-particle energy of the least bound occupied orbital. In the Hartree-Fock scheme, the single-particle energy ϵ_0 identifies with the Fermi energy ϵ_F . According to Koopmans' theorem [58], ϵ_0 is also equal to minus the one-nucleon separation energy $S_N = E_0^{N-1} - E_0^N$, where E_0^N is the ground state energy of the N -body system at the HF level⁽³⁾. As a result, long density tails arise for weakly bound systems with $S_N \rightarrow 0$. A measure of the spatial extension of the density is given by its radial moments $\langle r^n \rangle$. At long distances, the dominant contribution to $\langle r^n \rangle$ comes from ϕ_0 , whose associated moment $\langle r^n \rangle_0$ can be split into inner \mathcal{I}_n and outer \mathcal{O}_n parts :

$$\begin{aligned} \langle r^n \rangle_0 &= 4\pi \int_0^R |\bar{\phi}_0(r)|^2 r^{n+2} dr \\ &\quad + 4\pi \int_R^{+\infty} |\bar{\phi}_0^\infty(r)|^2 r^{n+2} dr \\ &\equiv \mathcal{I}_n + \mathcal{O}_n. \end{aligned} \quad (4)$$

The inner integral is finite by construction, whereas a further splitting of \mathcal{O}_n into two pieces, shows that, in the limit of weak binding $\epsilon_0 \rightarrow 0$, $\langle r^n \rangle_0$ (i) diverges as $\epsilon_0^{\frac{2l-1-n}{2}}$ for $n > 2l-1$ (ii) diverges as $\ln(\epsilon_0)$ for $n = 2l-1$ (iii) remains finite for $n < 2l-1$ [56]. In particular, one finds that the wave function normalization $\langle r^0 \rangle_0$ diverges for s waves, whereas the second moment $\langle r^2 \rangle_0$ diverges for both s and p waves. As a result, the root-mean-square (r.m.s.) radius, defined as :

$$R_{rms} = \sqrt{\frac{\langle r^2 \rangle}{\langle r^0 \rangle}}, \quad (5)$$

diverges for $\epsilon \rightarrow 0$ when ϕ_0 corresponds to a s or p wave. It diverges as $\epsilon_0^{-\frac{1}{2}}$ in the case of a s wave, and as $\epsilon_0^{-\frac{1}{4}}$ for a p wave. The centrifugal barrier confines wave functions with higher orbital momenta, in such a way that R_{rms} remains finite as $\epsilon_0 \rightarrow 0$ if ϕ_0 has an angular momentum $l \geq 2$.

According to this standard analysis, only low-lying s or p waves near the threshold are able to extend significantly outside the classically forbidden region. Their presence and occupation seem to be a prerequisite for the formation of neutron haloes. However, the second moment $\langle r^2 \rangle$ is only the leading order of the representation of the total density. Its expansion includes moments $\langle r^n \rangle$ of higher orders, which probe the nuclear density at increasing distances. Even if the higher-order moments weight usually little, one cannot rule out $l \geq 2$ -type halo structures yet, as $\langle r^n \rangle$ will also diverge for higher angular momentum states : $\langle r^4 \rangle$ will diverge for $l = 0, 1, 2$, $\langle r^6 \rangle$ will diverge for $l = 0, 1, 2, 3, \dots$ and so on.

B. Role of pairing correlations

Theoretical investigations of nuclei far from stability, either in non-relativistic [62, 63, 64] or relativistic [65, 66, 67] EDF frameworks, have pointed out the importance of pairing correlations. The treatment of static pairing correlations can be performed through the Hartree-Fock-Bogolyubov formalism, where the ground state energy is a functional of the hermitian one-body density matrix ρ and the skew symmetric pairing tensor κ , and reads⁽⁴⁾:

$$\begin{aligned} \mathcal{E}[\rho, \kappa, \kappa^*] &= \sum_{ij} t_{ij} \rho_{ji} + \frac{1}{2} \sum_{ij} \sum_{kl} \bar{v}_{iklj}^{\rho\rho} \rho_{ji} \rho_{lk} \\ &\quad + \frac{1}{4} \sum_{ik} \sum_{jl} \bar{v}_{iklj}^{\kappa\kappa} \kappa_{ik}^* \kappa_{jl}. \end{aligned} \quad (6)$$

In Eq. 6, t_{ij} denotes matrix elements of the one-body kinetic energy operator, whereas $\bar{v}_{iklj}^{\rho\rho}$ and $\bar{v}_{iklj}^{\kappa\kappa}$ are the two-body (antisymmetrized) matrix elements of the effective vertices in the particle-hole and particle-particle channels, respectively. The matrix elements of ρ and κ are defined as the normal and anomalous contractions :

$$\rho_{ij} = \langle \Phi | c_j^\dagger c_i | \Phi \rangle, \quad (7)$$

$$\kappa_{ij} = \langle \Phi | c_j c_i | \Phi \rangle, \quad (8)$$

where (c_k, c_k^\dagger) are fermionic creation and annihilation operators in configuration space. In the EDF approach, the auxiliary HFB state $|\Phi\rangle$ is meant to provide a one-body density mapping the exact one⁽⁵⁾, and takes the form of

⁴ Individual states have a good isospin projection, $q = n$ for neutrons or $q = p$ for protons, which is included in the general quantum number $k \equiv (k, q)$. The basis can be split into the two separated isospin components, as well as all matrices and fields involved. The isospin quantum number q will be made explicit only when necessary in the following.

⁵ See Appendix A 4 for the definition of the relevant one-body density.

³ If the center-of-mass contribution is removed, as it is usually done, corrections to Koopmans' theorem come into play [59, 60, 61].

a quasiparticle vacuum :

$$|\Phi\rangle = \prod_{\nu} \eta_{\nu} |0\rangle, \quad (9)$$

where $|0\rangle$ stands for the bare particle vacuum. The quasiparticles operators $(\eta_{\nu}, \eta_{\nu}^{\dagger})$ are introduced through the Bogolyubov transformation (U, V) [35, 68, 69, 70] :

$$\begin{cases} \eta_{\nu} = \sum_n (U_{n\nu}^* c_n + V_{n\nu}^* c_n^{\dagger}), \\ \eta_{\nu}^{\dagger} = \sum_n (V_{n\nu} c_n + U_{n\nu} c_n^{\dagger}). \end{cases} \quad (10)$$

The HFB equations of motion are obtained by minimizing the energy given by Eq. 6 with respect to $(\rho_{ij}, \rho_{ij}^*, \kappa_{ij}, \kappa_{ij}^*)_{i \leq j}$, under the constraint that the particle number is conserved in average. This leads to the eigenvalues problem :

$$\begin{pmatrix} h' & \Delta \\ -\Delta^* & -h'^* \end{pmatrix} \begin{pmatrix} U \\ V \end{pmatrix}_{\nu} = E_{\nu} \begin{pmatrix} U \\ V_e \end{pmatrix}_{\nu}, \quad (11)$$

where the Hartree-Fock field h' and the pairing field Δ are defined as :

$$h'_{ij} = h_{ij} - \lambda = \frac{\partial \mathcal{E}}{\partial \rho_{ji}} - \lambda, \quad \Delta_{ij} = \frac{\partial \mathcal{E}}{\partial \kappa_{ij}^*}, \quad (12)$$

$\lambda < 0$ being the chemical potential. Solutions of Eq. 11 are the quasiparticle eigenstates of the system $(U, V)_{\nu}$, with energy $E_{\nu} > 0$. Quasiparticle occupations are defined through the normalization of the lower components V_{ν} :

$$N_{\nu} = \sum_k |V_{\nu k}|^2 = \int |V_{\nu}(\vec{r})|^2 d\vec{r}. \quad (13)$$

In order to analyze the properties of the system, it is convenient to introduce the canonical basis $\{|\phi_i\rangle\}$ [35, 71]. In this basis, individual states can be grouped in conjugated pairs (l, \bar{l}) . The one-body density ρ is diagonal and the pairing tensor κ is in its canonical form :

$$\rho_{ij} \equiv v_i^2 \delta_{ij}, \quad (14)$$

$$\kappa_{ij} \equiv u_i v_i \delta_{ij}, \quad (15)$$

where $u_i = u_{\bar{i}} > 0$ and $v_i = -v_{\bar{i}}$ play the role of BCS-like coefficients, v_i^2 being the canonical occupation number. It is convenient to use the canonical basis to provide a single-particle picture and define individual energies and pairing gaps as :

$$e_i \equiv h_{ii}, \quad (16)$$

$$\Delta_i \equiv \Delta_{ii}. \quad (17)$$

In the presence of pairing, the asymptotics of the one-body neutron density is different from what it is in the HF scheme. The decay constant κ_0 is modified by

pairing correlations and becomes $\kappa_0 = \sqrt{\frac{-2m\epsilon_0}{\hbar^2}}$, with $|\epsilon_0| = E_0 - \lambda$, where $E_0 = \min_{\nu} [E_{\nu}]$ is the lowest quasiparticle excitation energy. Even for canonical states lying at the Fermi level at the drip-line ($e_0 \approx \lambda \approx 0$), one has $E_0 \approx \Delta_0 \geq 0$. Therefore, in first approximation, paired densities decrease faster than unpaired ones. In other words, pairing correlations induce an *antihalo effect* by localizing the density [72, 73].

Recently, the study of weakly bound nuclei using non self-consistent HFB methods with a central Wood-Saxon potential have shown that this effect could be ineffective under extreme conditions [74, 75, 76]. Indeed, very weakly bound $s_{1/2}$ states (bound by a few keVs) tend to decouple from the pairing field, due to their abnormal extension. As a consequence, the r.m.s. radius of such an unpaired orbital may diverge as in the HF scheme, leading to the formation of a halo. Although this possibility should be considered in principle, the depicted situation of a s orbit bound by a few keVs right at the drip-line would be highly accidental in realistic nuclei. This will be discussed in REF. [55].

Halo properties of drip-line nuclei have already been studied in various isotopic chains using self-consistent mean-field models [77, 78, 79, 80, 81, 82, 83, 84, 85]. In particular, the concept of giant halo has recently been introduced, where contributions from many low-lying orbitals with large r.m.s. radii sum up to form supposedly giant exotic structures [77]. Such a vision has been characterized within relativistic and non-relativistic pictures [81, 82, 83, 84, 85], mainly for Zr and Ca isotopes, because of the presence of low orbital momentum $l = 1$ states close to the Fermi level at the drip-line. Presence of more than two weakly bound orbitals have led to predicting the existence of giant haloes composed of six to eight neutrons. Those results are intuitively surprising, since the enhancement of collectivity in medium-mass nuclei is expected to decrease the chance to see spatially decorrelated nucleons. We will come back to this point.

C. Test cases : Cr and Sn isotopes

Chromium and tin isotopic chains are chosen as testing cases. Study of halo-type structures in other drip-line isotopes (Ca, Fe, Ni, Zr, Ti, Pb...) and systematics over ~ 500 "spherical" nuclei will be presented in REF. [55]. Calculations are performed using the non-relativistic HFB spherical code HFBRAD [86]. In HFBRAD, the space is discretized within a sphere of 40 fm radius, using vanishing boundary conditions for the wave functions (Dirichlet conditions). Convergence of the calculations as a function of numerical parameters will be commented on later, and has been checked in the case of the results which are presented here. The Skyrme SLy4 functional [87, 88] is employed in the particle-hole channel. The particle-particle effective vertex is a density-

dependent delta interaction corresponding to a "mixed-type" pairing. Its form factor is a compromise between a pairing which is constant over the nucleus volume ("volume-type"), and one which is peaked at the nucleus surface ("surface-type") [89, 90, 91, 92, 93]. To avoid divergences due to the local nature of the pairing functional, a phenomenological regularization scheme corresponding to a smooth cut-off at 60 MeV in the single-particle equivalent spectrum is used [63]. Such a pairing functional will be referred to as DFTM. More details about the Skyrme and pairing functionals used will be given in REF. [55].

The HFB problem is solved self consistently, so the "depth" and "width" of the central potential cannot be manually adjusted to reduce the binding energy of weakly bound states. Thus, potential halo candidates have to be found among realistic nuclei, the elementary criterion for halo candidates being the presence of low-lying low- l orbitals near the Fermi energy at the neutron drip-line, by analogy with the situation in lighter systems.

1. Chromium isotopes

Chromium isotopes ($Z = 24$) at the neutron drip-line are among the best halo candidates [55] among all predicted spherical medium-mass nuclei [94, 95]. In FIG. 1, the least bound neutron canonical energies e_i are plotted along the isotopic chain, ^{80}Cr being the predicted drip-line nucleus. The presence of low-lying $3s_{1/2}$ and $2d_{5/2}$ orbitals at the drip-line provides ideal conditions for the formation of halo structures.

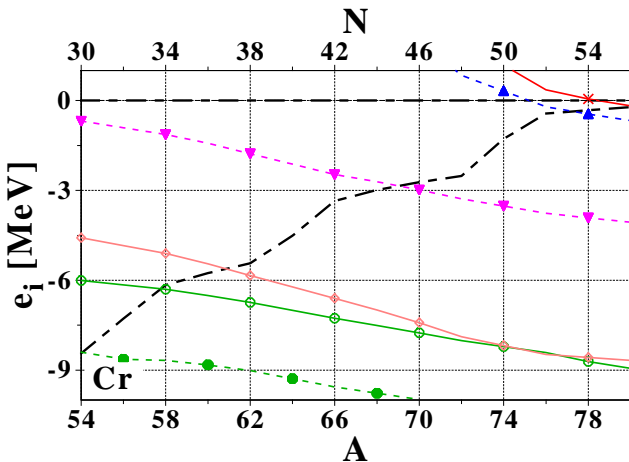


Figure 1: Neutron canonical energies e_i along the Cr isotopic chain, obtained through spherical HFB calculations with the $\{\text{SLy4+DFTM}\}$ functionals. Conventions for individual states used in all the figures of this paper are given in TAB. I

As discussed in SEC. II A, the abnormal extension of the one-body neutron density is usually characterized through the evolution of the neutron r.m.s. radius as one

l	$s_{1/2}$	$p_{1/2}$	$p_{3/2}$
0	×		
1		○	○
2	△		△
3		◊	◊
4	▽		▽
5		○	○
6	□		□

l	$d_{3/2}$	$f_{5/2}$	$d_{5/2}$
0			
1			
2			
3			
4			
5			
6			

l	$g_{7/2}$	$g_{9/2}$	$f_{7/2}$
0			
1			
2			
3			
4			
5			
6			

l	$h_{9/2}$	$h_{11/2}$	$g_{9/2}$
0			
1			
2			
3			
4			
5			
6			

l	$i_{11/2}$	$i_{13/2}$	$h_{11/2}$
0			
1			
2			
3			
4			
5			
6			

Fermi Level

Table I: Conventions used in all the figures for the labeling of individual states.

approaches the drip-line, which is presented in FIG. 2. A significant kink in the neutron r.m.s. is seen at the $N = 50$ shell closure. Such a kink is usually interpreted as a signature of the emergence of a neutron halo [77, 79]. However, this could equally be due to a shell effect. Indeed, as the $N = 50$ gap is crossed, the two-neutron separation energy drops, as seen in FIG. 3. Thus, the decay constant κ_0 of the one-body density is largely reduced. However, a genuine halo phenomenon relates to the existence of a region which spatially decorrelates from a core. Even though the present case looks very favorable as S_{2N} drops to almost zero, this cannot be thoroughly addressed in general by looking only at the evolution of the r.m.s. radii.

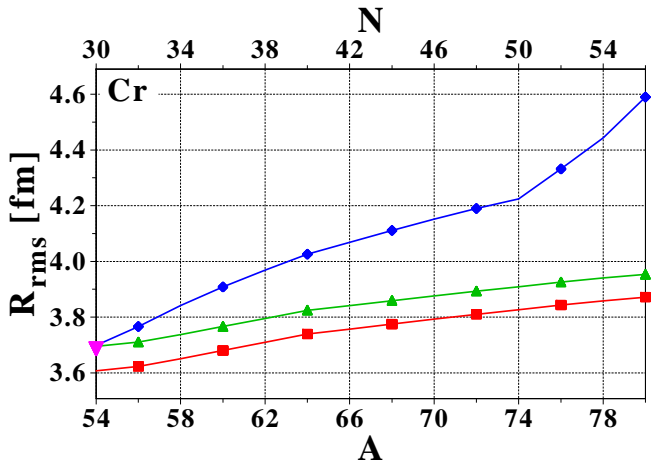


Figure 2: Same as FIG. 1 for proton (■), neutron (◆) and charge (▲) r.m.s. radii. Experimental values for charge r.m.s. radii are indicated when available (▼), along with experimental error bars [96].

2. Tin isotopes

Sn isotopes ($Z = 50$) have always been considered as a milestone for mean-field methods. Because of the magic proton number, they are rather easy to produce in ra-

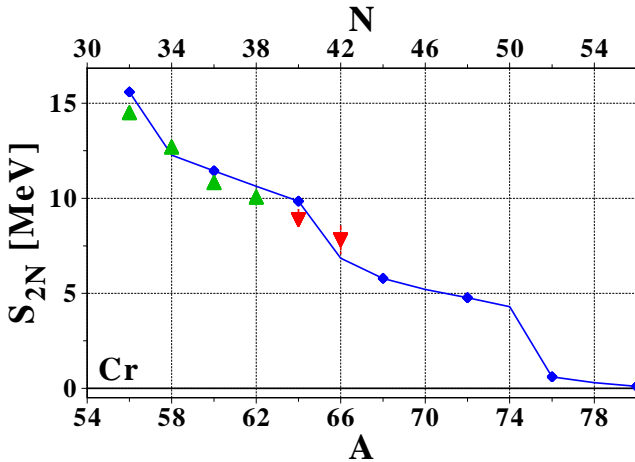


Figure 3: Same as FIG. 1 for two-neutron separation energies S_{2N} (\blacklozenge). Experimental values are indicated when available [97] (\blacktriangle when both masses are known, \blacktriangledown when at least one comes from mass extrapolation), along with experimental error bars.

radioactive beam facilities. Properties of two doubly-magic tin isotopes, ^{100}Sn and ^{132}Sn , are established and sometimes used in the fitting procedure of Skyrme functionals or Gogny interactions [36]. Also, the long isotopic chain is convenient for systematic studies. At the neutron drip-line, corresponding to ^{174}Sn for the {SLy4+DFTM} parameter set, the least-bound orbitals are mostly odd-parity states, among which $3p_{3/2}$ and $3p_{1/2}$ states might allow a halo-type structure to develop (FIG. 4).

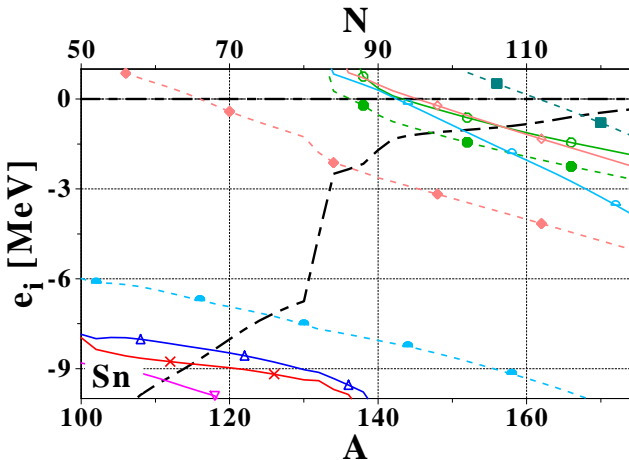


Figure 4: Same as FIG. 1 for neutron canonical energies of Sn isotopes.

However (i) the $l = 1$ states are relatively well bound (ii) the least bound orbital is the $1i_{13/2}$ ($l = 6$) intruder state, which can hardly overcome the centrifugal barrier to create a halo structure. Nevertheless, the neutron r.m.s. radius (FIG. 5) exhibits a weak kink at the $N = 82$ shell closure, which has been interpreted as a halo signature [79].

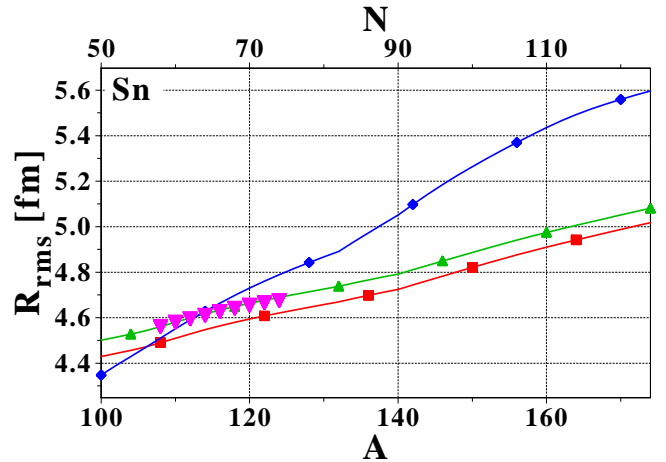


Figure 5: Same as FIG. 2 for proton, neutron and charge r.m.s. radii of Sn isotopes.

However, and as pointed out before, an analysis based on r.m.s. radii only is somewhat incomplete/misleading. Indeed, although the shell effect at the $N = 82$ magic number is related to a sudden decrease of the two-neutrons separation energy, the latter does not drop to zero at this point, as seen in FIG. 6. A direct connection between the r.m.s. kink and the formation of a neutron halo is very dubious.

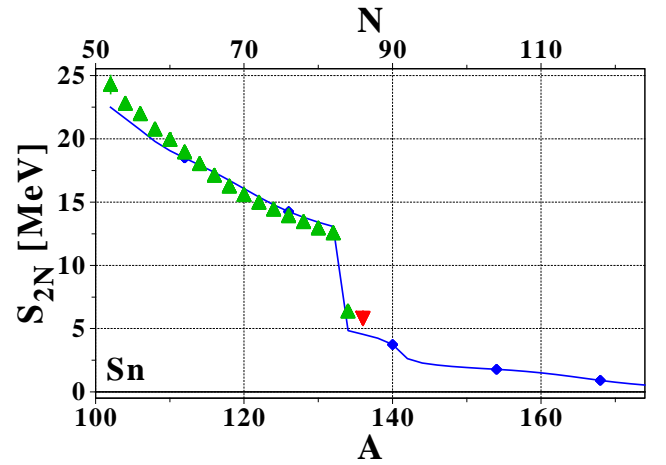


Figure 6: Same as FIG. 3 for two-neutron separation energies of Sn isotopes.

Characterization of haloes through the definition of neutron matter thickness and one-neutron region thickness is possible [80], but remains arbitrary and correlated to a one-neutron halo hypothesis. Another possible way is to extract so-called "halo factors" from the individual spectrum through antiproton annihilation probing the nuclear density extension [78, 98]. However, such tools do not allow the extraction of quantitative properties, such as the actual number of nucleons participating. They also define the halo as the region where the neutron

density dominates the proton one, which is an admixture of the neutron skin and the (potential) halo. An other method, which is expected to allow a more quantitative analysis, is now reviewed in more details.

D. The Helm model

1. Overview

The original purpose of the Helm model, introduced in REFS. [99, 100, 101] for the analysis of electron scattering on even-even nuclei, was to fit the experimental charge density using a few-parameter anzatz. The normalized nuclear charge density was approximated by the convolution of a sharp-sphere density of radius R_0 defining the nuclear extension, and a gaussian smoothing profile of width σ describing the surface thickness :

$$\rho_H(\vec{r}) = \rho_0 \int f_g(\vec{r} - \vec{r}') \Theta(R_0 - |\vec{r}'|) d\vec{r}', \quad (18)$$

where Θ is the Heaviside function, and :

$$\begin{cases} f_g(\vec{r}) = \frac{1}{(2\pi)^{3/2}\sigma^3} e^{-\frac{r^2}{2\sigma^2}}, \\ \rho_0 = \frac{3}{4\pi R_0^3}. \end{cases} \quad (19)$$

The invariance of EQ. 18 under an arbitrary rotation ensures that the Helm density ρ_H is spherical : $\rho_H(\vec{r}) = \rho_H(r)$. Its Fourier transform, the form factor $F_H(\vec{k}) = F_H(k)$, is analytical and reads as :

$$F_H(k) = \int \rho_H(\vec{r}) e^{i\vec{k}\cdot\vec{r}} d\vec{r} = \frac{3}{R_0 k} j_1(kR_0) e^{-\frac{\sigma^2 k^2}{2}}. \quad (20)$$

The r.m.s. radius of the Helm density only depends on R_0 and σ and reads as :

$$R_{rms}^H = \sqrt{\frac{\int \rho_H(r) r^4 dr}{\int \rho_H(r) r^2 dr}} = \sqrt{\frac{3}{5} (R_0^2 + 5\sigma^2)}. \quad (21)$$

This model has been used to study neutron skins and haloes in medium-mass nuclei close to the neutron drip-line [79]. Proton and neutron densities were defined as a superposition of a core density ρ_{core}^q plus a tail density ρ_{tail}^q describing, when necessary, the halo. The idea was to reproduce the core part ρ_{core}^q using the Helm anzatz ρ_H^q from EQ. 18, normalized to the nucleon number N^q ($N^q = N$ or Z). The two free parameters (R_0^q, σ^q) were adjusted on the high momentum part of the realistic form factor $F^q(k) = 4\pi \int \rho^q(r) r^2 j_0(kr) dr$, where $\rho^q(r)$ is the density coming out of the calculations. It was suggested in REF. [79] to evaluate (i) R_0^q through the first zero k_1^q of the realistic form factor : $R_0^q = \frac{z_1^1}{k_1^q}$, where z_1^1 is the

first zero of the Bessel function j_1 ($z_1^1 \approx 4.49341\dots$) (ii) σ^q by comparing the model and realistic form factors at their first extrema k_M^q (a minimum in the present case). This led to :

$$\sigma^q = \sqrt{\frac{2}{k_M^q} \ln \left(\frac{3N^q j_1(k_M^q R_0)}{R_0 k_M^q F^q(k_M^q)} \right)}. \quad (22)$$

Then, the following radii are defined (i)

$$R_{geom}(q) = \sqrt{\frac{5}{3}} R_{rms}(q) \text{ (geometric radius) for realistic densities (ii)} \quad R_{Helm}(q) = \sqrt{\frac{5}{3}} R_{rms}^H(q) = \sqrt{R_0^q + 5\sigma^q} \text{ (Helm radius) for model densities.}$$

Adjusting the parameters to the high momentum part of the realistic form factor was meant to make the fitting procedure as independent of the asymptotic tail of $\rho^q(r)$ as possible. Therefore, $R_{Helm}(n)$ should not incorporate the growth of $R_{geom}(n)$ when the neutron separation energy drops to zero and the spatial extension of weakly bound neutrons increases dramatically. In addition, it was found that the difference between $R_{Helm}(p)$ and $R_{geom}(p)$ was negligible near the neutron drip-line. From these observations, the neutron skin and neutron halo contributions to the geometric radius were defined as⁽⁶⁾ :

$$\begin{cases} \Delta R_{skin} = R_{Helm}(n) - R_{Helm}(p), \\ \Delta R_{halo} = R_{geom}(n) - R_{Helm}(n). \end{cases} \quad (23)$$

2. Limitations of the Helm model

Proton and neutron Helm radii are compared to the geometric ones on FIG. 7 for chromium and tin isotopes. The behavior of $R_{geom}(q)$ and $R_{Helm}(q)$ for Sn isotopes is the same as in REF. [79]⁽⁷⁾. For both isotopic chains, the sudden increase of the neutron geometric radius after the last neutron shell closure might be interpreted as a signature of a halo formation. However, ΔR_{halo} is non-zero along the entire Cr isotopic chain, even on the proton-rich side. The latter result is problematic since no neutron halo is expected at the proton drip-line.

The latter can be understood as a direct consequence of the gaussian folding in the definition of the Helm density

⁶ Similar definitions could be applied to nuclei close to the proton drip-line, where a proton halo is expected instead of a neutron one.

⁷ Results slightly differ from REF. [79] because of the different pairing functional and regularization scheme used, as well as the larger number of j -shells taken into account in the present calculations. The influence of limiting the number of j shells in the calculations will be discussed in REF. [55].

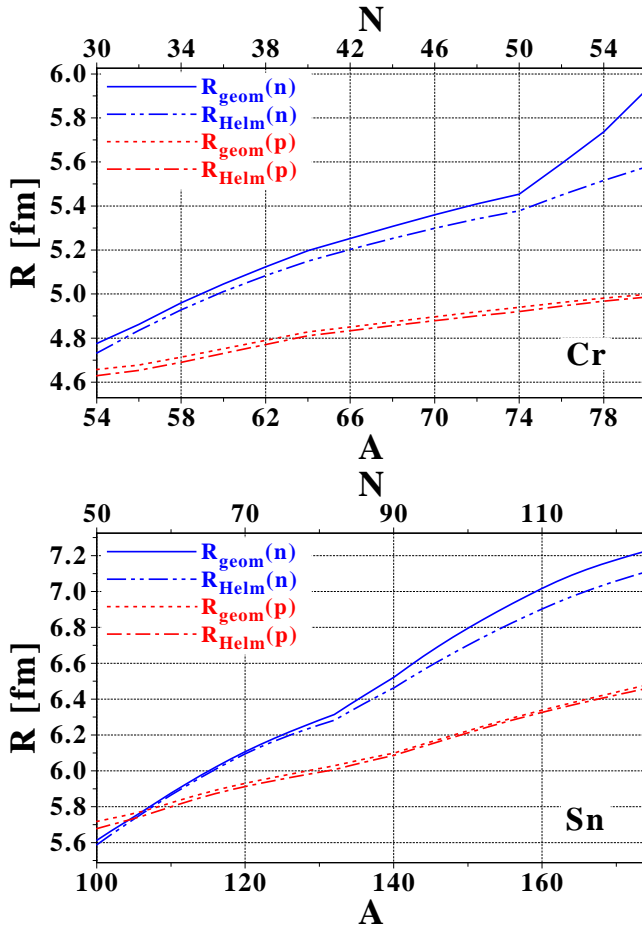


Figure 7: Geometric and Helm radii for Cr (top panel) and Sn (bottom panel) isotopes calculated in the spherical HFB approach with the {SLy4+DFTM} functionals.

(Eq. 18). The asymptotic decay of the Helm density is roughly quadratic in logarithmic scale, whereas a linear decay is expected [62, 63, 102]. To illustrate this point, FIG. 8 displays the realistic and Helm densities of ^{54}Cr (in the valley of stability) and ^{80}Cr (drip-line nucleus). The different asymptotic behaviors is obvious here. The Helm densities are unable to reproduce the correct long-range part of the non-halo proton density, or the neutron density of nuclei in the valley of stability.

The difference in the asymptotics leads to unsafe predictions for the halo parameters ΔR_{halo} because skin and halo cannot be properly separated with this method. Thus, one may put into question the accuracy of the Helm model to analyze halo properties. Such problems, as well as a lack of flexibility to account for finer details of the nuclear density had already been pointed out in relation with electron-electron scattering experiments [103].

One might then also question the fitting procedure introduced in REF. [79]. The method naturally requires R_0^q and σ^q to be adjusted on the form factor at sufficiently large k to relate to the "core" part of the density only. For these reasons, the procedure proposed in REF. [79] seems

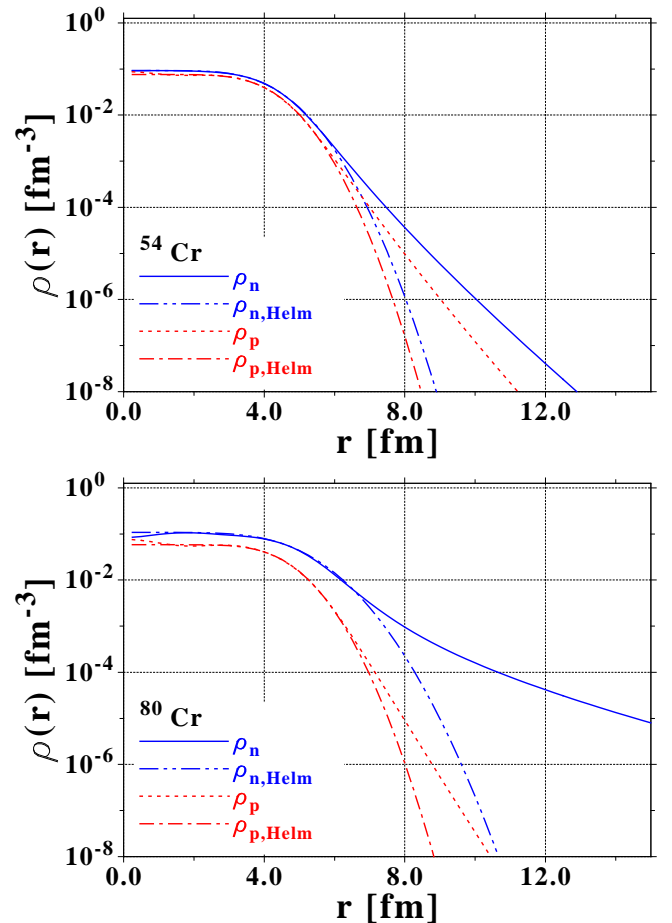


Figure 8: Realistic (solid lines) and Helm (dashed-dotted lines) densities of ^{54}Cr and ^{80}Cr .

to be a good compromise at first. But other choices can be made, such as using the second zero k_2^q of $F^q(k)$ to adjust R_0^q . Following such arguments, four slightly different fits, all consistent with the general idea exposed above, have been tested to check the stability of the Helm model :

$$\begin{aligned}
 A_1 &: F_H^q(k_1^q) = F(k_1^q), F_H^q(k_M^q) = F^q(k_M^q)^{(8)}, \\
 A_2 &: F_H^q(k_1^q) = F^q(k_1^q), F_H^q(k_1^q) = F^q(k_1^q), \\
 A_3 &: F_H^q(k_2^q) = F^q(k_2^q), F_H^q(k_2^q) = F^q(k_2^q), \\
 A_4 &: F_H^q(k_1^q) = F^q(k_1^q), F_H^q(0.4 k_1^q) = F^q(0.4 k_1^q)^{(9)}.
 \end{aligned}$$

FIG. 9 shows the halo parameter ΔR_{halo} obtained for Cr isotopes using protocols A_1 to A_4 . Although the general pattern remains unchanged, the halo parameter significantly depends on the fitting procedure used to

⁸ This is the standard procedure from REF. [79].

⁹ This method includes more of the long distance part of the realistic density.

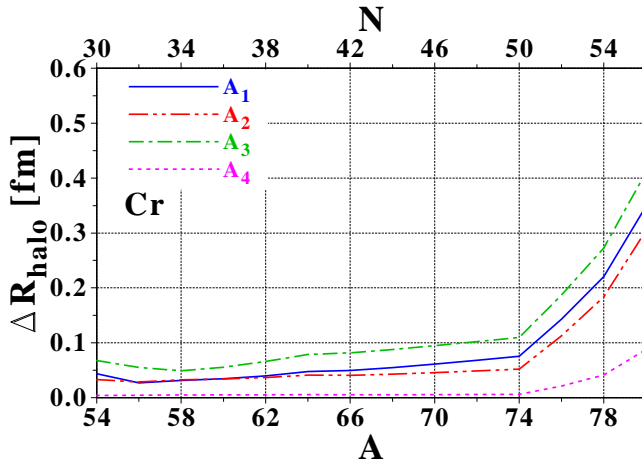


Figure 9: Halo parameter ΔR_{halo} for chromium isotopes using different fitting procedures for the Helm parameters (R_0^q, σ^q) (see text).

determine (R_0^q, σ^q) . Because of the wrong asymptotics of the Helm density discussed above, one cannot make ΔR_{halo} to be zero for magic and proton-rich nuclei (cf. protocol A_4), keeping unchanged its values for halo candidates at the neutron drip-line⁽¹⁰⁾. In addition, such a procedure would require an *a priori* knowledge of reasonable halo candidates.

As a next step, we tried to use other trial densities to improve the standard Helm model. However, a key ingredient is to have an analytical expression of the associated form factor, which is then adjusted on the realistic one. We could not find any expression for the convolution product leading to analytical expressions of F_H^q and to good asymptotics, with only two free parameters⁽¹¹⁾. Finally, adjusting the model density on the realistic one in coordinate space to capture those missing asymptotics would also rely on an arbitrary *a priori* separation of the density into core and tail contributions.

Although the Helm model looked promising at first, we have shown the versatility of its predictions. The inability of the model to describe the correct asymptotics of the nuclear density in the valley of stability, as well as the too large freedom in the fitting procedure, limit very much its predictive power. Therefore a more robust analysis method is needed to characterize medium-mass halo nuclei.

¹⁰ The Helm densities obtained with the A_4 protocol still do not match the realistic ones, even for protons.

¹¹ Using model densities depending on three free parameters would make the Helm model even more dependent on the fitting procedure.

III. NEW CRITERION FOR A QUANTITATIVE ANALYSIS OF HALO SYSTEMS

Although deceiving, the previous attempts have underlined the following point : an accurate method must characterize haloes through the existence of a *spatially* decorrelated component in the nucleon density. We propose in the following a method which allows the extraction of such a contribution to the one-body density in a model-independent way. Our starting point is a thorough analysis of the one-body density. Characterizing halo structures requires in particular an accurate description and understanding of the asymptotic behavior of the latter. Such an analysis is performed in SEC. III A. Applications of this model-independent characterization to mean-field HF and HFB methods is presented in SEC. III B. Finally, in SEC. III C, the previous properties are used to define the halo region as well as new quantitative criteria.

A. Properties of the one-body density

1. Definitions and notations

Complete derivations of the results and additional properties of the quantities introduced in the following can be found in Appendix A. The main results are summarized here.

Let us start from the exact non-relativistic N -body Hamiltonian⁽¹²⁾ :

$$H^N = \sum_{i=1}^N \frac{p_i^2}{2m} + \sum_{\substack{i,j=1 \\ i < j}}^N V(r_{ij}), \quad (24)$$

where $r_{ij} = |\vec{r}_i - \vec{r}_j|$ and V denotes the bare nucleon-nucleon interaction. H^N is invariant under translation and can be decomposed into a center-of-mass $H_{\text{c.m.}}^N$ and an intrinsic part H_{intr}^N . Thus, eigenstates of H^N , denoted by $\Psi_{i,\vec{K}}^N(\vec{r}_1 \dots \vec{r}_N)$, can be factorized into the center-of-mass part (plane wave) times the intrinsic wave function :

$$\Psi_{i,\vec{K}}^N(\vec{r}_1 \dots \vec{r}_N) = e^{i\vec{K} \cdot \vec{R}_N} \Phi_i^N(\vec{\xi}_1 \dots \vec{\xi}_{N-1}), \quad (25)$$

where \vec{K} is the total momentum and \vec{R}_N the center-of-mass position :

$$\vec{R}_N = \frac{1}{N} \sum_{i=1}^N \vec{r}_i. \quad (26)$$

¹² The Coulomb interaction is omitted here, as the focus is on neutron haloes. The spin degrees of freedom are also not explicitly included, but their introduction would not change the final results. Finally, the Hamiltonian is restricted to a two-body vertex. The conclusions would not change either with the introduction of the missing three-body force, because of its short range.

The intrinsic wave function Φ_i^N is expressed using the $N - 1$ independent Jacobi coordinates :

$$\vec{\xi}_i = \vec{r}_{i+1} - \frac{1}{i} \sum_{j=1}^i \vec{r}_j, \quad (27)$$

which are invariant under translation, and is associated with the intrinsic energy E_i^N .

The ground-state intrinsic wave function Φ_0^N can be expanded in terms of the complete orthonormal set of intrinsic $(N - 1)$ -body wave functions $\{\Phi_\nu^{N-1}\}$, which are eigenstates of the $(N - 1)$ -body intrinsic Hamiltonian [104, 105, 106, 107] :

$$H_{intr}^{N-1} \Phi_\nu^{N-1}(\vec{r}_1 \dots \vec{r}_{N-1}) = E_\nu^{N-1} \Phi_\nu^{N-1}(\vec{r}_1 \dots \vec{r}_{N-1}), \quad (28)$$

such that :

$$\Phi_0^N(\vec{r}_1 \dots \vec{r}_N) = \frac{1}{\sqrt{N}} \sum_\nu \Phi_\nu^{N-1}(\vec{r}_1 \dots \vec{r}_{N-1}) \times \varphi_\nu(\vec{r}_N - \vec{R}_{N-1}). \quad (29)$$

The states Φ_ν^{N-1} are ordered by increasing intrinsic energies, $\nu = 0$ corresponding to the ground state of the $(N - 1)$ -body system. The normalization of the overlap functions provides the so-called spectroscopic factors [108, 109] :

$$S_\nu = \int d\vec{r} |\varphi_\nu(\vec{r})|^2. \quad (30)$$

For large distances $r > R$, the nuclear interaction vanishes and the asymptotic radial part $\bar{\varphi}_\nu$ of the overlap functions becomes solution of the free Schrödinger equation with a reduced mass $m^* = \frac{N-1}{N}m$:

$$\left[\left(\frac{d^2}{dr^2} + \frac{2}{r} \frac{d}{dr} - \frac{l_\nu(l_\nu + 1)}{r^2} \right) - \kappa_\nu^2 \right] \bar{\varphi}_\nu^\infty(r) = 0, \quad (31)$$

with $\kappa_\nu = \sqrt{-\frac{2m^*\epsilon_\nu}{\hbar^2}}$, where $\epsilon_\nu = (E_0^N - E_\nu^{N-1})$ is minus the one-nucleon separation energy to reach Φ_ν^{N-1} . Solutions of the whole free Shrödinger equation take the form :

$$\varphi_\nu^\infty(\vec{r}) = \sqrt{B_\nu} h_{l_\nu}(i\kappa_\nu r) Y_{l_\nu}^{m_\nu}(\theta, \varphi). \quad (32)$$

Finally, the relevant object to be defined for self-bound systems is the intrinsic one-body density matrix [106, 110, 111] :

$$\rho_{[1]}(\vec{r}, \vec{r}') = \sum_\nu \varphi_\nu^*(\vec{r}') \varphi_\nu(\vec{r}), \quad (33)$$

which shows that the intrinsic one-body density matrix is completely determined by the overlap functions [110].

One can extract the intrinsic one-body density $\rho_{[1]}(\vec{r})$ as the local part of the intrinsic density matrix :

$$\rho_{[1]}(\vec{r}) = \sum_\nu |\varphi_\nu(\vec{r})|^2 = \sum_\nu \frac{2l_\nu + 1}{4\pi} |\bar{\varphi}_\nu(r)|^2, \quad (34)$$

where the energy degeneracy associated with the orbital momentum has been resolved through the summation of the spherical harmonics.

2. Asymptotic behavior

According to Eqs. 32 and 34, the intrinsic one-body density behaves asymptotically as⁽¹³⁾ :

$$\rho_{[1]}^\infty(r) = \sum_\nu \frac{B_\nu^2}{4\pi} (2l_\nu + 1) |h_{l_\nu}(i\kappa_\nu r)|^2. \quad (35)$$

The intrinsic one-body density at large distances is a superposition of energy- and l -dependent individual components. For very large arguments, Eq. 3 shows that the squared modulus of a Hankel function behaves as $\frac{e^{-2\kappa_i r}}{(\kappa_i r)^2}$.

Thus the $\nu = 0$ component dominates and provides the usual asymptotic behavior [62, 63, 102]⁽¹⁴⁾ :

$$\rho_{[1]}^\infty(r) \approx \frac{B_0^2}{4\pi} (2l_0 + 1) \frac{e^{-2\kappa_0 r}}{(\kappa_0 r)^2}. \quad (36)$$

The very asymptotic form of the Hankel function is independent of the angular momentum⁽¹⁵⁾. As a result, the contributions of the overlap functions to $\rho_{[1]}^\infty$ are ordered according to their corresponding separation energies $|\epsilon_\nu|$. However, corrections to this ordering at smaller distances come from (i) the l -dependence of the Hankel functions due to the centrifugal barrier, which favors low angular momentum states (ii) the $(2l + 1)$ degeneracy factor which favors high angular momentum states. Again, for extremely large distances the least bound component will always prevail, although this may happen beyond simulation reach⁽¹⁶⁾. To characterize the net effect of corrections (i) and (ii), the contributions $(2l_\nu + 1)|h_{l_\nu}(i\kappa_\nu r)|^2$,

¹³ Rigorously, this is true only if the convergence of the overlap functions to their asymptotic regime is uniform in the mathematical sense, i.e. if they reach the asymptotic regime at a common distance R [110]. This is not actually proven in nuclear physics, but has already been shown in atomic physics [112, 113] for the electron charge density.

¹⁴ Note that the asymptotics of ρ^p and ρ^n are different because of the charge factor (Hankel functions for neutrons, Whittaker functions for protons).

¹⁵ This explains why high order moments $\langle r^n \rangle$ of the density diverge when high- l states are loosely bound, as it was observed in SEC. II A.

¹⁶ For instance, if a $l=6$ component is less bound than a $l=0$ one by only 5 keV, it is only beyond $r=100$ fm that the former becomes the leading component in the asymptotic density.

for a fixed energy but different angular momenta, are compared in FIG. 10 for the solutions of a simple finite spherical well. Outside the well, Hankel functions are exact solutions of the problem. The potential depth is adjusted to obtain identical eigenenergies for all l_ν . The $(2l_\nu + 1)$ factor reduces the gap between s and p components. However, the effect of the centrifugal barrier is the strongest for large r , where individual states are ordered according to l_ν , favoring low angular momenta. In the end, the separation energy remains the leading factor as far as the ordering of overlap functions at long distances is concerned.

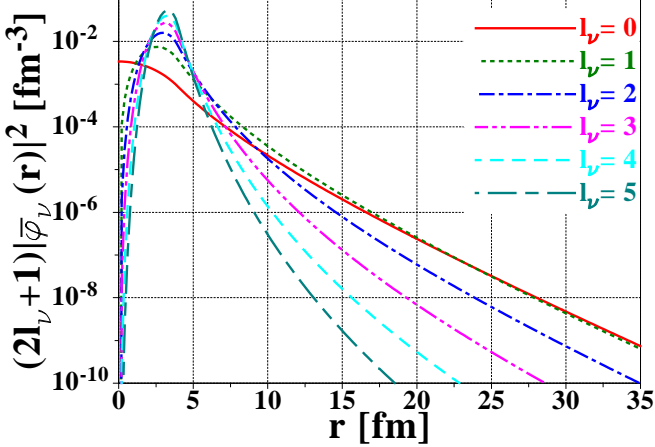


Figure 10: Squared components of the solutions of a finite spherical well of fixed width $a = 4$ fm, multiplied by the spherical degeneracy factor $(2l+1)$, for various angular momenta and fixed energy $\epsilon = -100$ keV. The first state for each l_ν (nodeless component corresponding to a primary quantum number equal to 0) is represented.

3. Consequences on the one-body density

The ordering of the individual components in $\rho_{[1]}^\infty$ has interesting consequences on the properties of the density as a whole. Indeed, if normalized overlap functions $\psi_\nu(\vec{r})$ are introduced, EQ. 34 becomes :

$$\rho_{[1]}(r) = \sum_\nu \frac{2l_\nu + 1}{4\pi} S_\nu |\bar{\psi}_\nu(r)|^2 \equiv \sum_\nu C_\nu(r). \quad (37)$$

Let us take all spectroscopic factors equal to 1 for now. The $\nu = 0$ component, corresponding to the smallest separation energy, dominates at large distances. Because of continuity ($\bar{\psi}_\nu(r) \in \mathcal{L}^2(\mathbb{R}^+)$) and normalization conditions, this implies that $\bar{\psi}_0(r)$ has to cross all the other overlap functions as r goes inward from $+\infty$ to 0. The position at which $\bar{\psi}_0$ crosses each $\bar{\psi}_\nu$ depends on the difference of their separation energies and angular momenta. In particular, there will exist a crossing between $\bar{\psi}_0(r)$ and the remaining density

$\sum_{\nu \geq 1} C_\nu(r)$. The same situation is encountered when considering $\bar{\psi}_1(r)$: it will cross the remaining density $[\rho^{[1]}(r) - C_0(r) - C_1(r)]$ etc... The centrifugal barrier will influence the position of such crossings but not their occurrence, because of the robustness of the (very) asymptotic ordering discussed in the previous section.

Let us now incorporate the effect of spectroscopic factors. Qualitatively, S_ν is known to increase with the excitation energy of the corresponding eigenstate of the $(N - 1)$ -body system. Thus, the normalization of φ_0 is smaller than those of the excited components φ_ν , which mechanically ensures the existence of the crossings discussed previously. A similar reasoning holds when going from φ_0 to φ_1 etc...

One should finally pay attention to the number of nodes of $\bar{\varphi}_\nu(r)$. This effect actually favors low angular momentum states as far as the asymptotic positioning is concerned : if two components have the same energy but different angular momenta, the one with the lowest l will have a greater number of nodes (according to Hund's rule), and contribution from its central part to the total normalization is reduced. That is, the weight of the asymptotic tail is increased, which favors its domination at long distance. However, this effect is expected to have a small impact in comparison with the other disturbances discussed in the previous section. As a result, the occurrence of crossings between the components of the density is not jeopardized by the existence of nodes in the overlap functions.

B. Applications

In the previous section, the energies at play denote exact nucleon separation energies. No approximation to the nuclear many-body problem has been involved so far. As a result, the results obtained are fully general and model-independent. In practice however, one uses an approximate treatment of the N -body problem. Let us briefly discuss how the previous analysis translates into HF and HFB schemes.

First, an important clarification regarding the physical interpretation of the quantities at play in the calculations must be carried out. Indeed, the laboratory wave functions used in EDF approaches based on the HF or HFB methods are *auxiliary* states built in a way that the one-body density intends to map the exact intrinsic density. The HF/HFB states $|\Phi\rangle$ explicitly break the translational invariance of the system. The one-body density is then calculated through the laboratory density operator, as defined by EQ. A15, and maps the exact intrinsic one-body density. Important issues are raised by this

mapping procedure⁽¹⁷⁾. Additionally, in standard DFT, the Kohn-Sham implementation of the Hohenberg-Kohn theorem ensures that (only) the least bound Kohn-Sham energy $|\epsilon_0|$ relates to the exact separation energy. Rearrangement terms come into play for other Kohn-Sham energies. One usually assumes that all $|\epsilon_\nu|$ constitute a good zeroth order approximation to exact separation energies between the N -body ground state and states in the $(N-1)$ -body system.

1. Hartree-Fock case

In the HF implementation of the EDF approach, spectroscopic factors are either 0 or 1, and behave according to a step function $S_\nu = \Theta(\epsilon_F - \epsilon_\nu)$. The HF single-particle states ϕ_ν are the canonical states, and identify with the intrinsic overlap functions φ_ν , thus $\epsilon_\nu \equiv e_\nu$. The one-body density reads :

$$\rho(r) = \sum_{\nu=1}^N \frac{2l_\nu + 1}{4\pi} |\bar{\phi}_\nu(r)|^2, \quad (38)$$

where the sum over ν can be truncated to the N lowest energy states. The HF functions being solutions of the one-body Schrödinger equation given by Eq. 1, the analysis presented in the previous section for the intrinsic density directly applies.

2. Hartree-Fock-Bogolyubov case

In the HFB formalism, the one-body density can be evaluated using either the canonical states ϕ_i or the lower components V_ν of the quasiparticle spinors :

$$\rho(r) = \sum_i \frac{2l_i + 1}{4\pi} v_i^2 |\bar{\phi}_i(r)|^2 = \sum_\nu \frac{2l_\nu + 1}{4\pi} |\bar{V}_\nu(r)|^2. \quad (39)$$

The eigenstates of the $(N-1)$ -body system are described as one-quasiparticle states on top of the fully paired N -body ground state⁽¹⁸⁾, thus $|\epsilon_\nu| \equiv E_\nu - \lambda$. The overlap functions can be assimilated, through the mapping

¹⁷ Phenomenological nuclear EDF calculations of self-bound nuclei are not properly related to an exact Hohenberg-Kohn/Kohn-Sham-like scheme. In particular, many issues related to the present interpretation and the role of symmetry breaking must be clarified.

¹⁸ It can be shown that the perturbative one-quasiparticle state $\eta_n^\dagger |\Phi\rangle$ contains $N + u_n^2 - v_n^2$ particles in average if $|\Phi\rangle$ is constrained to N particles in average. It is only for deep-hole quasiparticle excitations ($v_n^2 \approx 1$) that the final state will be a good approximation of the $(N-1)$ -body system. The correct procedure is to construct each one-quasiparticle state self-consistently by breaking time-reversal invariance, and requiring $(N-1)$ particles in average [114, 115]. The overlap functions and spectroscopic factors could be computed numerically in such a context.

discussed above, to the lower component of the quasiparticle wave functions. Thus, the spectroscopic factors S_ν identify with the quasiparticle occupations N_ν as defined by Eq. 13. This shows that HFB-based EDF approaches explicitly incorporate some effects of the spreading of the single-particle strength in the quasiparticle approximation [116].

The function $S_\nu = f(|\epsilon_\nu|)$, whose typical behavior is presented in FIG. 11 for ^{80}Cr , takes continuous values between 0 and 1. The difference between hole-like quasiparticle excitations and particle-like ones is visible. Indeed, S_ν increases with $|\epsilon_\nu|$ for hole-like excitations. They constitute the main branch which tends to a step function when correlations are not explicitly included, like in the HF-based EDF approach. On the other hand, spectroscopic factors of particle-like quasiparticle excitations go to zero for high-lying excitations.

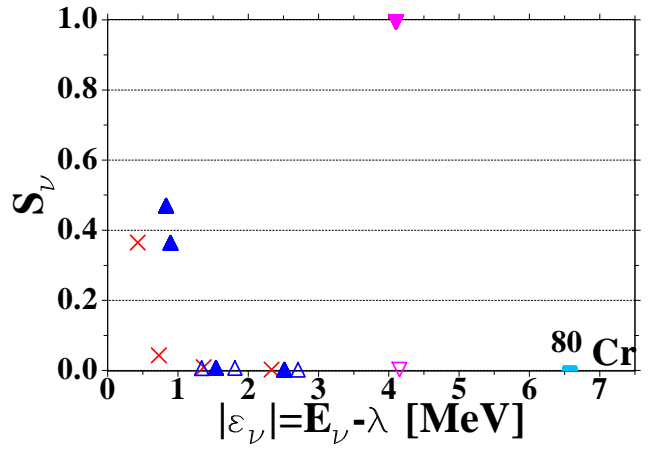


Figure 11: Neutron quasiparticles occupation as a function of the equivalent HFB energy in the ^{80}Cr , calculated with the $\{\text{SLy4+DFTM}\}$ functionals. The conventions from TAB. 1 are used for labeling individual quasiparticle states. Only quasiparticles with occupations greater than 10^{-3} are displayed.

C. Halo Characterization

1. Definition

The discussion of SEC. III A 3 shows how the individual contributions to the one-body density position themselves with respect to each other. This is now used to characterize halo systems. As pointed out earlier, the most simple and general definition of a halo relates to the existence of nucleons which are spatially decorrelated from the others, constituting the "core". This can only be achieved if some contributions to the intrinsic density exhibit very long tails. Also, "delocalization from the core" requires the latter to remain well localized. Those properties can be understood in terms of crossings between weakly bound components and well-bound ones in

the one-body density. To achieve a spatial decorrelation between a core and a tail part, crossings between two groups of orbitals with very different asymptotic slopes have to occur. *This will translate into a sharp crossing and a pronounced curvature in the density.* Such a crossing is illustrated in FIG. 12 for a simple model where the halo is due to a single state. Of course, more complex situations have to be considered where multiple states contribute to the core and the halo. Indeed, the enhancement of collectivity in medium-mass systems implies that one does not expect a single state to be well separated from the others.

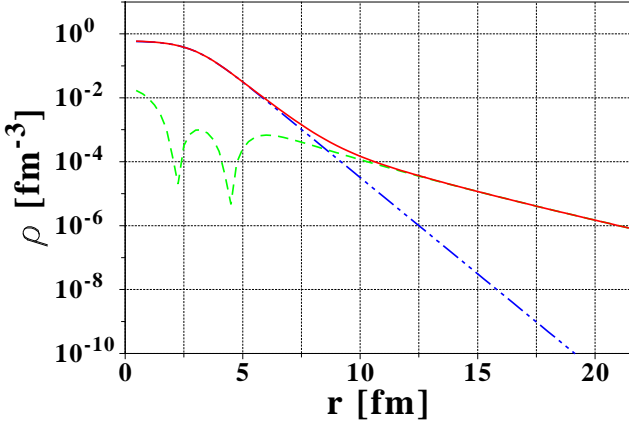


Figure 12: "Core+tail" simplified model. The total density (solid line) is the superposition of a core contribution (dashed line) and a halo one (dash-dotted line). A semi-phenomenological density (see Appendix B) is used for the core density, whereas the halo part is the realistic $3_{1/2}^+$ state of ^{80}Cr obtained from spherical HFB calculations with the {SLy4+DFTM} functionals.

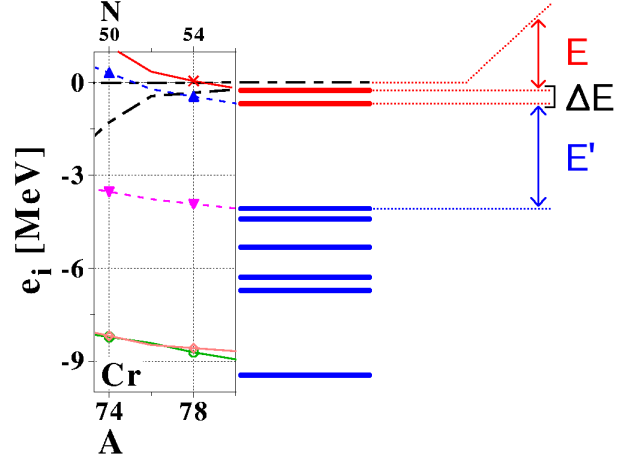
2. Relevant energy scales

The need for an abrupt change of slope in the density provides crucial conditions for the existence of halo structures, which translate into specific patterns in the excitation energy spectrum of the $(N-1)$ -body system. Firstly, to extend out far away, the least bound component φ_0 must have a very small separation energy. Second, several components $\varphi_1, \varphi_2 \dots \varphi_m$ may contribute significantly to the density tail if they all have separation energies of the same order as φ_0 . Third, for those tails to be spatially decorrelated from the rest of the density (the "core"), the components with $\nu > \nu_m$ have to be much more localized than those with $\nu \leq \nu_m$. This condition is fulfilled when the crossing between the m^{th} and $(m+1)^{\text{th}}$ components in the density is sharp, which corresponds to very different decay constants $\kappa_m \ll \kappa_{m+1}$ at the crossing point.

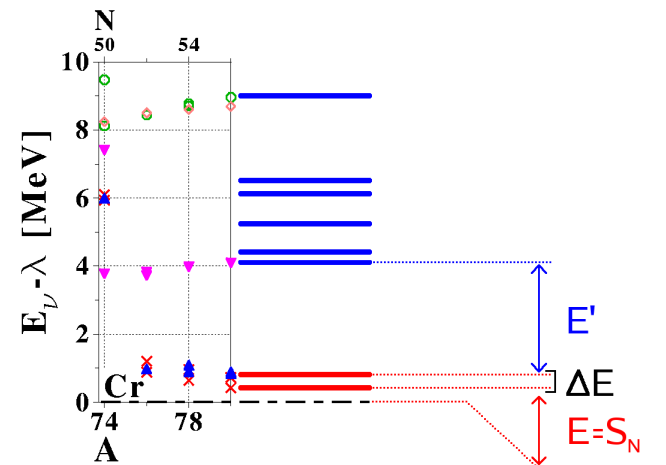
This suggests that a halo appears when (i) the one-neutron separation energy $S_N = |\epsilon_0|$ is close to zero (ii)

a bunch of low energy states in the $(N-1)$ -body system have separation energies $|\epsilon_\nu|$ close to zero (iii) a significant gap in the spectrum of the $(N-1)$ -body system exists, which separates the latter bunch of states φ_ν from higher excitations.

A very similar discussion was proposed in connection with Effective Field Theory for weakly bound nuclei [117], where two energy scales (E, E') were found relevant : (i) the nucleon separation energy $E = S_N$ which drives the asymptotic behavior of the one-body density (ii) the core excitation energy $E' = |\epsilon_{m+1}|$ which needs to be such as $E' \gg E$, in order for the tail orbitals to be well decorrelated from the remaining core. One additional energy scale that we presently identify is the energy spread ΔE of the low-energy low-lying states, which becomes relevant when more than one component is involved in the halo. The latter analysis is displayed in FIG. 13 and is also translated in terms of mean-field canonical energies e_i .



(a) Canonical neutron energy spectrum e_i .



(b) Separation energy spectrum $|\epsilon_\nu|$ for the $(N-1)$ -body system.

Figure 13: Energy scales relevant for the appearance of haloes (right-hand sides). The realistic spectra obtained through HFB calculations of the last chromium isotopes are shown on the left-hand sides.

In the end, the ideal situation for the formation of a halo is : (i) a very small separation energy, in orders of a few hundred keVs. The empirical value of $2 \text{ MeV}/A^{2/3}$ from REFS. [29, 30] gives a good approximation of expected values in halo systems (ii) a narrow bunch of low-lying states, whose spread ΔE should not exceed $\sim 1 \text{ MeV}$ (ii) a large gap E' with the remaining states, at least 4 or 5 times the separation energy E . Those are only qualitative values, and obviously there is not sharp limit between halo and non-halo domains.

3. Characterization of the halo region

As discussed in the previous section, a halo will be characterized by a pronounced ankle in the density, due to the sharp crossing between the aggregated low-lying components and the remaining ones. This ankle translates into a peak in the second derivative of the log-density, as seen in FIG. 14 for a schematic case.

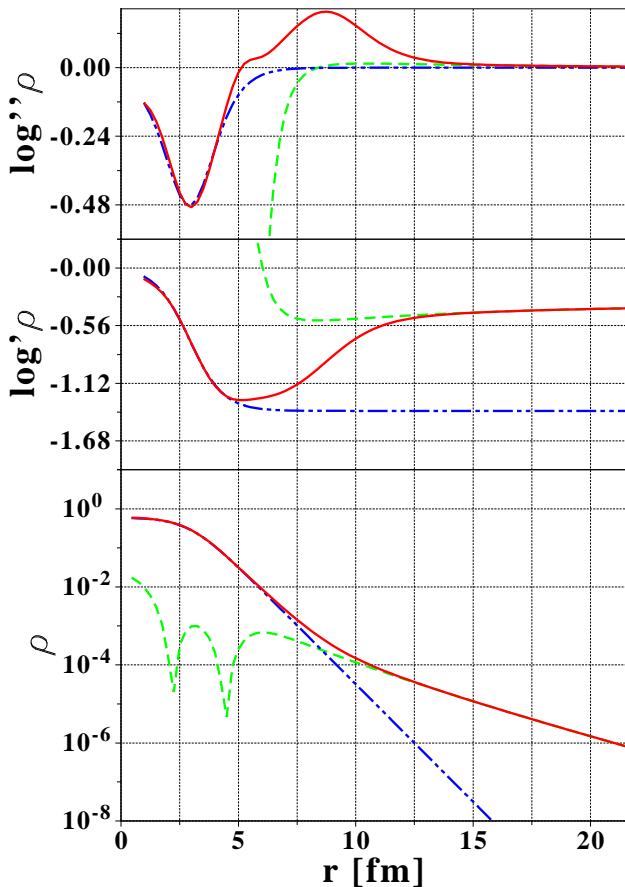


Figure 14: The ankle of the log-density due to the presence of a low-lying state well separated from the remaining ones : log-density (bottom panel), first (middle panel) and second (top panel) log-derivatives. The conventions are the same as in FIG. 12.

At the position $r = r_{max}$ of the maximum of the peak, core and tail aggregated contributions cross, that is they contribute equally to the total density. At larger radii, the halo, if it exists, dominates. Therefore, *we define the decorrelated region as the region beyond the radius r_0 where the core density is one order of magnitude smaller than the halo one*. However the latter definition poses two practical problems. First, in realistic calculations, one only accesses the total density. Second, the choice of one order of magnitude is somewhat arbitrary.

Many simulations have been performed to locate r_0 unambiguously, using either one or several contributions to the halo density, and covering large energy ranges for E , E' and ΔE . More details on the method used to find the best approximation for r_0 , as well as corresponding theoretical error bars, are given in Appendix B. It has been found that r_0 can be solidly defined through :

$$\begin{cases} r_0 > r_{max}, \\ \frac{\partial^2 \log \rho(r)}{\partial r^2} \Big|_{r=r_0} = \frac{2}{5} \frac{\partial^2 \log \rho(r)}{\partial r^2} \Big|_{r=r_{max}}, \end{cases} \quad (40)$$

as exemplified in FIG. 15. Also, error bars on the determination of r_0 are introduced, such as :

$$0.35 \leq \frac{\log''(\rho(r_0))}{\log''(\rho(r_{max}))} \leq 0.50. \quad (41)$$

Once validated by simulations, the method only relies on the density as an input, and does not require an *a priori* separation of the one-body density into a core and a halo. Finally, one may note that our definition of the halo region does not exclude contributions from components with angular momenta greater than 1, and the results for realistic systems will be "as it".

4. Halo criteria

We now introduce several criteria to characterize the halo in a quantitative way. First, the average number of nucleons in the halo region can be extracted through :

$$N_{halo} = 4\pi \int_{r_0}^{+\infty} \rho(r) r^2 dr. \quad (42)$$

Another important information is the effect of the halo region on the radial moments of the density. By definition of r_0 , the contribution of the core to any moment $\langle r^n \rangle$ is negligible for $r \geq r_0$ ⁽¹⁹⁾, and the following quantity can be used to evaluate the effect of the decorrelated region

¹⁹ It has been checked in the case of the r.m.s. radius, and is all the more true as n increases.

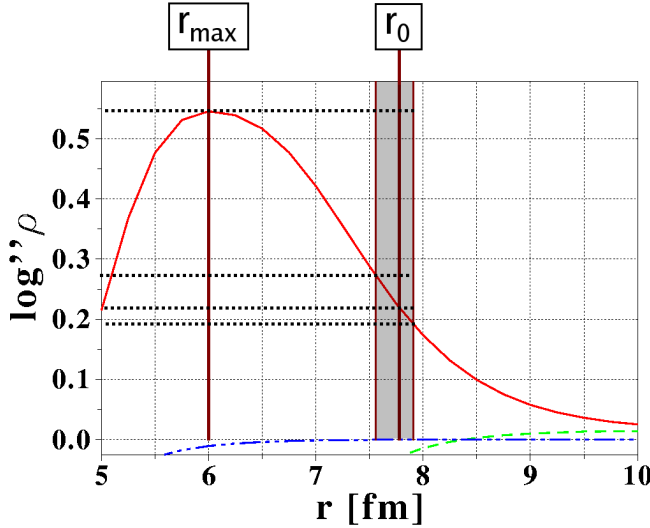


Figure 15: Definition of r_0 through the second derivative of the log-density, using the same model density as in FIG. 14. The shaded area corresponds to the tolerance margin (error bars) on r_0 (see text).

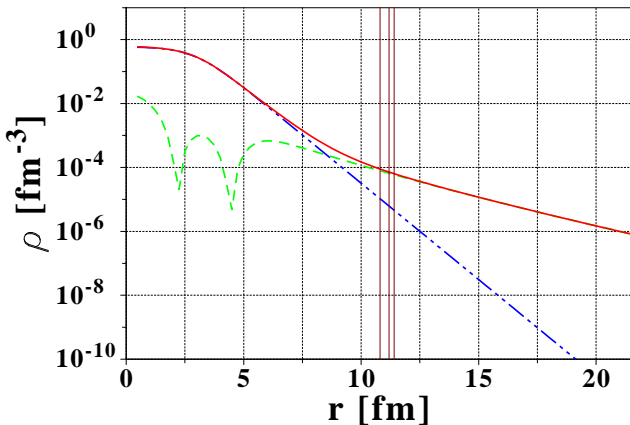


Figure 16: Consequences of the definition of r_0 (center vertical line - see text) in the same model as in FIG. 14. The halo density dominates the core part by one order of magnitude.

on the nuclear extension :

$$\delta R_{halo} = R_{rms,tot} - R_{rms,inner}$$

$$= \sqrt{\frac{\int_0^{+\infty} \rho(r) r^4 dr}{\int_0^{+\infty} \rho(r) r^2 dr}} - \sqrt{\frac{\int_0^{r_0} \rho(r) r^4 dr}{\int_0^{r_0} \rho(r) r^2 dr}}. \quad (43)$$

δR_{halo} is similar to ΔR_{halo} defined in the case of the Helm model (Eq. 23). However, it does not rely on any *a priori* decomposition of the density into a core and a halo part. Extensions to all radial moments of the density

can be envisioned⁽²⁰⁾.

The error bars on r_0 propagate to error bars on N_{halo} and δR_{halo} . Obviously N_{halo} and δR_{halo} are correlated. However they do not carry exactly the same information, and are both relevant. The latter feature will strongly manifest itself when dealing with systematic calculations over the nuclear landscape [55].

In the case of stable/non-halo nuclei, both quantities will be extremely small. There is still a slight curvature in the density profile for such nuclei, which translates into a very broad peak in the second log-derivative, but the r_0 value will be large and will define a region where the density is extremely low. This is illustrated by FIG. 17, where r_0 is plotted for chromium isotopes as a function of A . The maximum of r_0 is attained for the magic shell $N = 50$, which shows that the decorrelated region appears for very large distances in the case of expected non-halo nuclei.

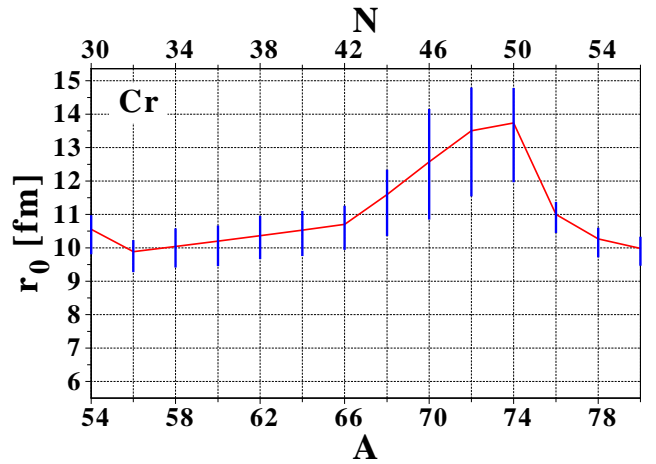


Figure 17: Evolution of r_0 along the Cr isotopic chain, obtained through spherical HFB calculations with the {Sly4+DFTM} functional.

Given the theoretical model/approximation of interest, further characterization of the halo can be achieved by looking at the individual contributions of each overlap function :

$$N_{halo,\nu} = 4\pi(2l_\nu + 1) \int_{r_0}^{+\infty} |\bar{\varphi}_\nu(r)|^2 r^2 dr. \quad (44)$$

$N_{halo,\nu}$ provides a decomposition of the halo in terms of single-particle-like states. Note that the part of each overlap function for $r < r_0$ naturally does not contribute to halo observables.

²⁰ Numerical issues appear when going to high order moments. Indeed, $\langle r^n \rangle$ is more and more sensitive to the upper limit of integration as n increases. Thus, the result may significantly depend on the box size used to discretize the continuum in HFB calculations, or on numerical limits in the case of simulations.

By analogy with the criterion used for light halo systems, the probability of each individual overlap function φ_ν to be in the $r \geq r_0$ region can also be defined :

$$P_\nu = \frac{\int_{r_0}^{+\infty} |\bar{\varphi}_\nu(r)|^2 r^2 dr}{\int_0^{+\infty} |\bar{\varphi}_\nu(r)|^2 r^2 dr}. \quad (45)$$

IV. FIRST RESULTS

We apply the analysis method introduced in SEC. III to the results of realistic self-consistent HFB calculations of chromium and tin isotopes.

A. Implementation of the criteria

In the code HFBRAD, the HFB problem is solved on a spatial mesh of step size $\Delta r = 0.25$ fm. For the 40 fm box that we consider, the mesh has 160 points in the radial direction, for both the individual wave functions and the densities. To obtain a satisfactory precision, the second order log-derivative is computed using a five-points difference formula [118]. The precision of the formula is then the same as the intrinsic precision of the Numerov algorithm used for the integration of second-order differential equations (which is $\mathcal{O}(\Delta r^6)$) [86, 119]. Approximate positions of the maximum of the second order log-derivative of $\rho(r)$ and r_0 are first determined with a simple comparison algorithm. To increase the precision, 11-points polynomial spline approximations of the density and its second log-derivative around the two points of interest are performed. Because the functions involved are regular enough, a spline approximation provides a good precision on the value of the maximum of $\log''\rho(r)$, as well as on the value of r_0 , which are obtained using a dichotomy procedure up to a (arbitrary) precision of 10^{-5} . Finally, the integrations to compute N_{halo} and δR_{halo} are performed with the trapezoid method and a linear approximation of the density between each mesh points.

In the definition of δR_{halo} , the core contribution to the total r.m.s. is approximated as the root-mean-square radius of the density distribution truncated to its $r < r_0$ part. To check the influence of this cut, the core density was extrapolated beyond the point where the second order log-derivative crosses zero⁽²¹⁾ using the expression from Eq. 36, by enforcing continuity of ρ and ρ' . No difference was seen for δR_{halo} .

The individual contributions $N_{halo,i}$, as well as the individual probabilities P_i , are evaluated in the canonical basis. Equivalently, $N_{halo,\nu}$ and P_ν can be calculated in the quasiparticle basis. Quasiparticle states are the best approximation to the overlap functions, but canonical and quasiparticle basis really constitute two equivalent pictures. Indeed, each canonical state is, roughly speaking, split into different quasiparticles of similar energies. A summation of quasiparticle contributions of same quantum numbers in a given energy range would allow to recover the single-particle canonical approximation. The latter is preferred here, as it is more intuitive to work in the natural basis.

B. Cr isotopes

According to SEC. III C 1, drip-line chromium isotopes appear to be ideal halo candidates. The "separation energy" spectrum $|\epsilon_\nu| = E_\nu - \lambda$ to the states in the $(N - 1)$ -body system is shown in FIG. 18. TAB. II dis-

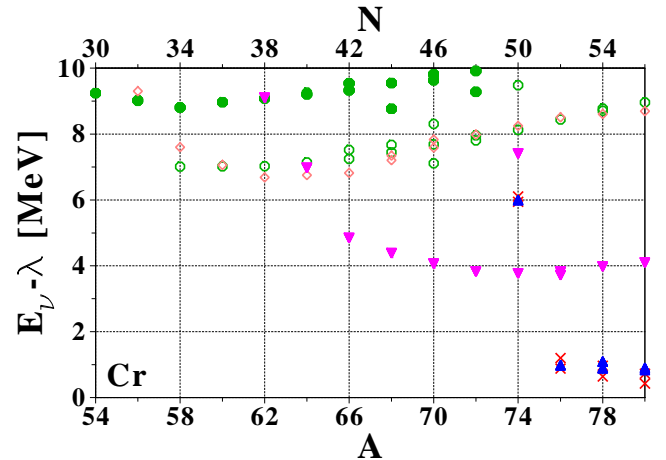


Figure 18: Neutron separation energies $|\epsilon_\nu| = E_\nu - \lambda$ along the Cr isotopic chain, obtained through spherical HFB calculations with the {Sly4+DFTM} functional. Only relevant quasiparticles energies ($N_\nu > 0.01$) are displayed. Conventions for labeling individual states are found in TAB. I.

plays the canonical and quasiparticle spectra for the drip-line nucleus ^{80}Cr . In the canonical basis, $|\epsilon_0|$ is about 180 keV, whereas two low-lying states ($3s_{1/2}$ and $2d_{5/2}$) are present with an energy spread $\Delta E \approx 500$ keV. They are separated from a core of orbitals by $E' \approx 3.5$ MeV. Equivalently, the separation energy in the quasiparticle basis is $|\epsilon_0| \approx 420$ keV, whereas four quasiparticle states, with an energy spread of $\Delta E \approx 470$ keV, are further separated from higher excited states by $E' \approx 3.2$ MeV. The separation energy S_N for ^{80}Cr is compatible with the phenomenological requirement for light halo nuclei of $2 \text{ MeV}/A^{2/3} \approx 137$ keV. The energy scales correspond to an ideal halo case, as discussed in SEC. III C 2.

²¹ This is the point where the halo contribution effect becomes significant.

Can. spectrum ^{80}Cr		Exc. spectrum ^{79}Cr	
	e_i (MeV)		$E_\nu - \lambda$ (MeV)
$E \uparrow$	> 0	$f_{5/2}$	> 10
$\Delta E \left\{ \begin{array}{l} 3s_{1/2} \\ 2d_{5/2} \end{array} \right.$	-0.178	$p_{1/2}$	8.694
E'	-0.670	$g_{9/2}$	8.960
$1g_{9/2}$	-4.062	$d_{5/2}$	4.103
$1f_{5/2}$	-8.676	$d_{5/2}$	0.893
$1f_{5/2}$	-8.676	$s_{1/2}$	0.832
$2p_{1/2}$	-8.942	$s_{1/2}$	0.728
	< -10	$E \uparrow$	0.427
			0

Table II: Neutron canonical energies e_i in ^{80}Cr and separation energies $|\epsilon_\nu| = E_\nu - \lambda$, as predicted by the {SLy4+DFTM} functionals. For the latter, states with a spectroscopic factor smaller than 10^{-2} are not included.

The criteria introduced in SEC. III C 1 are now applied. FIG. 19 shows the average number of nucleons participat-

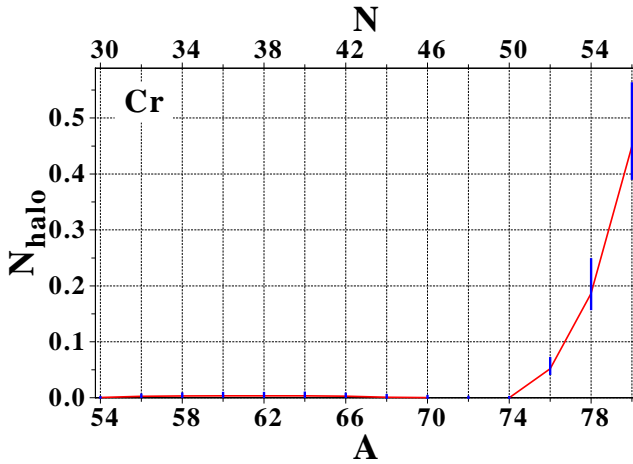


Figure 19: Average number of nucleons participating in the halo along the Cr isotopic chain, as a function of the nuclear mass, as predicted by the {SLy4+DFTM} functionals. Theoretical error bars are included (see text).

ing in the halo. Whereas N_{halo} is consistent with zero for $N \leq 50$, a sudden increase is seen beyond the $N = 50$ shell closure. The appearance of a decorrelated contribution to the density of the last three isotopes can be seen in the evolution of the neutron densities along the isotopic chain in FIG. 20. For $N \geq 50$, such a behavior translates into a non-zero value of N_{halo} . The quantitative effect remains small, as the decorrelated region is populated by ~ 0.45 nucleons in average in ^{80}Cr . This is small relative to the total neutron number. In absolute

however, N_{halo} is comparable to what is found in light s -wave halo nuclei like ^{11}Be , where roughly 0.4 nucleons constitute the decorrelated part of the density [120].

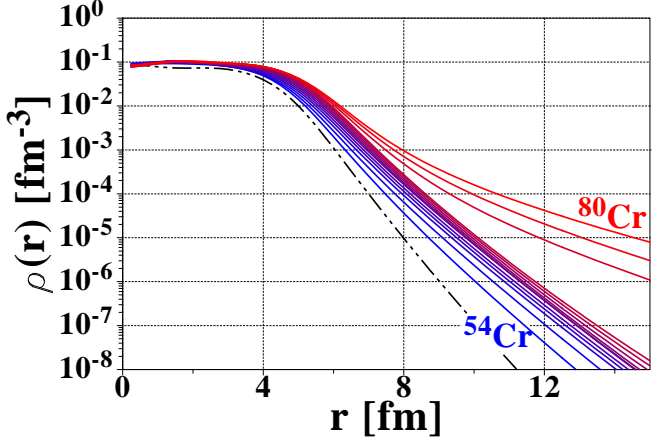


Figure 20: Neutron densities for even-even Cr isotopes, from ^{54}Cr to ^{80}Cr . The proton density of ^{54}Cr is given (dashed-dotted line) as a reference for the neutron skin.

The halo factor δR_{halo} is shown in FIG. 21 as a function of A . The halo contributes significantly to the total neutron r.m.s. radius (up to ~ 0.13 fm) after the $N = 50$ shell closure. The latter result corresponds to a splitting

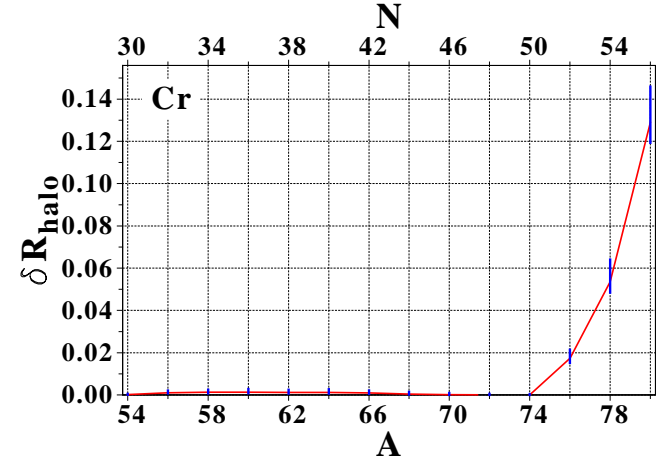


Figure 21: Halo factor parameter δR_{halo} in the Cr isotopic chain.

of the total r.m.s. radius into a core and a halo contribution, as displayed in FIG. 22. In comparison with the Helm model, shell effects are properly separated from halo effects as the core r.m.s. radius includes a kink after $N = 50$ because of the filling of less bound states. Only the physics related to the existence of truly decorrelated neutrons is extracted by N_{halo} and δR_{halo} .

To characterize further this halo region, individual contributions $N_{\text{halo},i}$ are evaluated. The results are summarized in TAB. III. As expected, the main contributions to the halo come from the most weakly bound states,

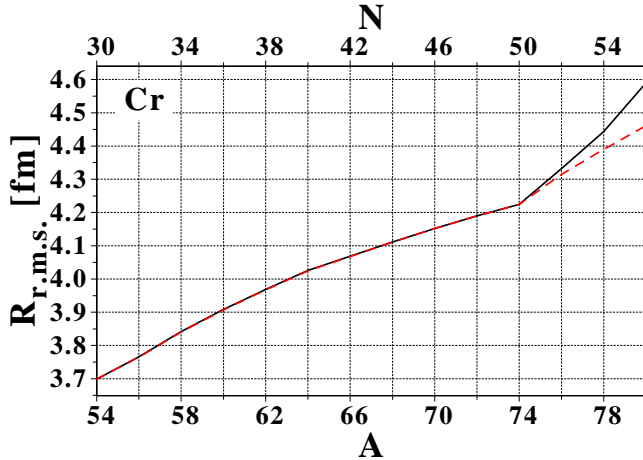


Figure 22: Total neutron root-mean-square radius (solid line) and core contribution (dashed line) for chromium isotopes, as predicted by the {SLy4+DFTM} functionals.

while for magic nuclei, like ^{74}Cr , all contributions are consistent with zero. At the neutron drip-line, important contributions are found from both $3s_{1/2}$ and $2d_{5/2}$ states. The $l = 2$ state contributes for almost 50% of the total number of nucleons in the decorrelated region, although this state is more localized than the $3s_{1/2}$ because of its binding energy and of the centrifugal barrier. The latter effects are compensated by a larger canonical occupation v_i^2 and a larger intrinsic degeneracy. This could not be expected from the standard qualitative analysis presented in SEC. II A and from the experience acquired in light nuclei.

Finally, the probability P_i to be in the outer region $r \geq r_0$ in ^{80}Cr is typical of halo systems for the $3s_{1/2}$, around 49%. It is a little bit lower for the $2d_{5/2}$ state because of the centrifugal barrier, around 26%.

We have found for Cr isotopes the apparition of a decorrelated region at the drip-line, after the $N = 50$ shell closure. This region contains an admixture of states (s and d waves in the present case), whose probabilities to be in the outer region $r \geq r_0$ are both compatible with the situation in light halo nuclei. We end up with the notion of *collective halo* building up at the neutron drip-line for Cr isotopes.

C. Sn isotopes

So far, prediction of haloes in tin isotopes after the $N = 82$ shell closure [79] have been based on the Helm model, whose limitations have been pointed out in SEC. II D 2. The robust analysis tools introduced in the present work are expected to give more reliable results. Neutron densities of Sn isotopes exhibit a qualitative change for $N > 82$, as seen in FIG. 23. However, the transition is smoother than in the case of chromium iso-

N_{halo}	^{74}Cr			
	$1.7.10^{-4}$			
e_i (MeV)	v_i^2	$N_{halo,i}$	P_i	
$3s_{1/2}$	+0.036	0.000	0.000	0.0%
$2d_{5/2}$	-0.024	0.000	0.000	0.0%
$1g_{9/2}$	-3.618	1.000	0.001	0.1%
$2p_{1/2}$	-8.100	1.000	0.000	0.0%
$1f_{5/2}$	-8.400	1.000	0.000	0.0%
<i>Other</i>	< -10.0	—	$\sim 1.7.10^{-4}$	—
N_{halo}	^{76}Cr			
	$5.2.10^{-2}$			
e_i (MeV)	v_i^2	$N_{halo,i}$	P_i	
$3s_{1/2}$	+0.356	0.050	0.007	14.8%
$2d_{5/2}$	-0.209	0.311	0.039	12.6%
$1g_{9/2}$	-3.764	0.991	0.002	0.2%
$2p_{1/2}$	-8.416	0.998	0.000	0.0%
$1f_{5/2}$	-8.477	0.998	0.000	0.0%
<i>Other</i>	< -10.0	—	$\sim 2.2.10^{-3}$	—
N_{halo}	^{78}Cr			
	0.186			
e_i (MeV)	v_i^2	$N_{halo,i}$	P_i	
$3s_{1/2}$	+0.052	0.147	0.045	30.4%
$2d_{5/2}$	-0.450	0.604	0.128	21.2%
$1g_{9/2}$	-3.919	0.991	0.005	0.5%
$1f_{5/2}$	-8.576	0.998	0.001	0.1%
$2p_{1/2}$	-8.714	0.998	0.001	0.1%
<i>Other</i>	< -10.0	—	$\sim 6.2.10^{-3}$	—
N_{halo}	^{80}Cr			
	0.450			
e_i (MeV)	v_i^2	$N_{halo,i}$	P_i	
$3s_{1/2}$	-0.178	0.421	0.207	49.3%
$2d_{5/2}$	-0.670	0.843	0.223	26.4%
$1g_{9/2}$	-4.062	0.995	0.008	0.8%
$1f_{5/2}$	-8.676	0.999	0.001	0.1%
$2p_{1/2}$	-8.942	0.999	0.002	0.2%
<i>Other</i>	< -10.0	—	$\sim 9.4.10^{-2}$	—

Table III: Contributions from the most weakly bound canonical orbitals to the number of nucleons in the decorrelated region for Cr isotopes at the drip-line, and probabilities for those states to be in the outer region $r \geq r_0$.

topes (FIG. 20), because of the enhanced collectivity.

TAB. IV displays the canonical and quasiparticle spectra for the drip-line nucleus ^{174}Sn . The energy scales involved are not compliant with the definition of a halo. In the canonical basis, the separation energy E is roughly 1.2 MeV, whereas six states with an energy spread $\Delta E \approx 3.8$ MeV are separated from a core of orbitals by a gap $E' \approx 5.5$ MeV. Equivalently in the quasiparticle basis one has $E \approx 1.5$ MeV. The four low-lying quasiparticles with a spread $\Delta E \approx 3.4$ MeV are separated from higher excitations by $E' \approx 5.6$ MeV.

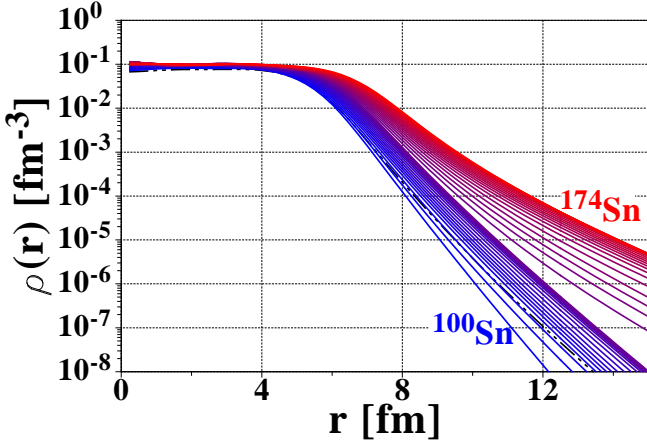


Figure 23: Same as FIG. 20 for the Sn isotopes. The "separation" occurs for $N = 82$. Proton density of ^{100}Sn is given as a reference in dashed-dotted line.

In particular, the energy spread of the low-lying states ΔE is too large to favor the formation of a halo. Also, according to the phenomenological criterion for light halo nuclei, the separation energy of ^{174}Sn should be of order of $2 \text{ MeV}/A^{2/3} \approx 64 \text{ keV}$ for a halo to emerge. As a reference, FIG. 24 shows the separation energies $|\epsilon_\nu|$ in tin isotopes.

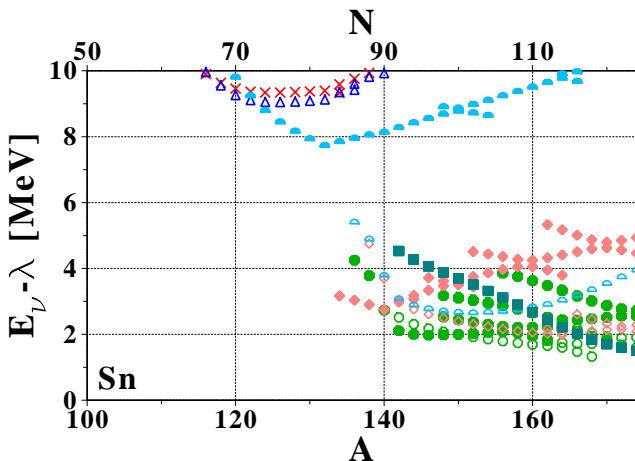


Figure 24: Same as FIG. 18 for neutron separation energies of Sn isotopes.

The N_{halo} parameter is displayed in FIG. 25. The maximum value of N_{halo} , around 0.18, is very small compared to the total number of nucleons. The absolute numbers are also smaller than the ones obtained in the case of the (lighter) Cr isotopes. An interesting feature is the decrease of N_{halo} for $N > 166$. This is a consequence of the filling of the highly degenerated $1i_{13/2}$ state at the drip-line (see FIG. 4) : as the number of nucleons occupying the $1i_{13/2}$ shell increases, the depth of the Hartree-Fock potential also increases and the shells become more

Can. spectrum 174		Exc. spectrum ^{173}Sn	
	e_i (MeV)		$E_\nu - \lambda$ (MeV)
E	> 0	$d_{5/2}$	14.169
ΔE	$1i_{13/2}$	$d_{3/2}$	12.026
	$3p_{1/2}$	$s_{1/2}$	11.967
	$2d_{5/2}$	$1h_{11/2}$	10.603
	$3p_{3/2}$		
	$1h_{9/2}$	E'	
	$2f_{7/2}$	$f_{7/2}$	4.937
E'	-1.208	$f_{7/2}$	4.463
	-1.855	$h_{9/2}$	3.890
	-2.227	$p_{3/2}$	2.722
	-2.665	$p_{1/2}$	2.648
	-3.823	$p_{3/2}$	2.559
	-5.014	$f_{5/2}$	2.290
		$f_{5/2}$	2.082
		$p_{1/2}$	1.905
		$p_{1/2}$	1.610
		$i_{13/2}$	1.502
		E	
	$1h_{11/2}$	-10.575	
	$2d_{3/2}$	-12.581	
	$3s_{1/2}$	-12.747	
	$2d_{5/2}$	-14.944	
		< -15	
			0

Table IV: Same as TAB. II for the neutron canonical energies of ^{174}Sn , and the associated separation energies $|\epsilon_\nu|$ of ^{173}Sn .

bound, thus more localized. This effect is another hindrance to the formation of haloes from low-lying high angular momentum states.

The second halo parameter δR_{halo} shown in FIG. 26 confirms that the decorrelated region has little influence on the nuclear extension, of the order of 0.02 fm. Its contribution is found to be much less than predicted by the Helm model. The collectivity in tin isotopes hinders the possibility of a sharp separation of core and tail contributions in the total density.

The analysis of single-particle contributions, summarized in TAB. V, confirms the latter result. First, the higher collectivity of the decorrelated region is observed, as $3p_{1/2}$, $3p_{3/2}$ and $2f_{7/2}$ ($l = 3$) states contribute roughly the same to N_{halo} . For higher angular-momentum orbitals, the effect of the centrifugal barrier is seen : the $1h_{9/2}$ and $1i_{13/2}$, the latter being the least bound orbital, do not contribute significantly to the total halo. Finally, individual probabilities P_i remain very small, and do not exceed a few percents.

For all those reasons, only an extended neutron skin

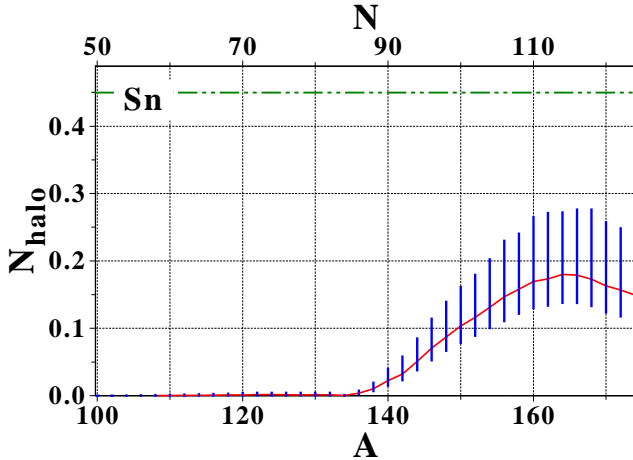


Figure 25: Average number of nucleons in the decorrelated/halo region for Sn isotopes. For comparison, $N_{halo}({}^{80}\text{Cr})$ is shown as a dashed-dotted line.

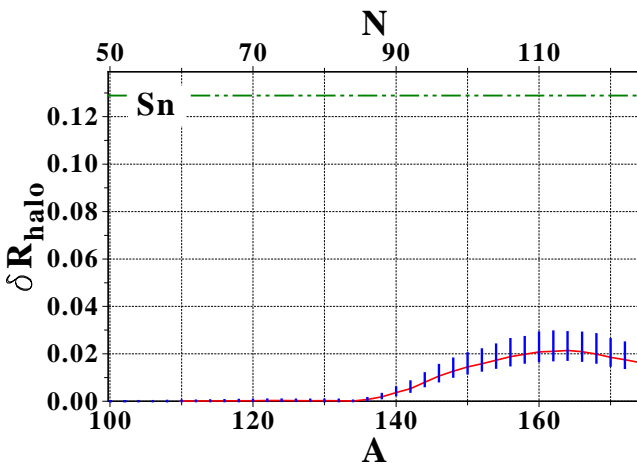


Figure 26: Halo factor parameter δR_{halo} in the Sn isotopic chain. For comparison purposes, the maximum δR_{halo} obtained for Cr isotopes is represented in dashed-dotted line.

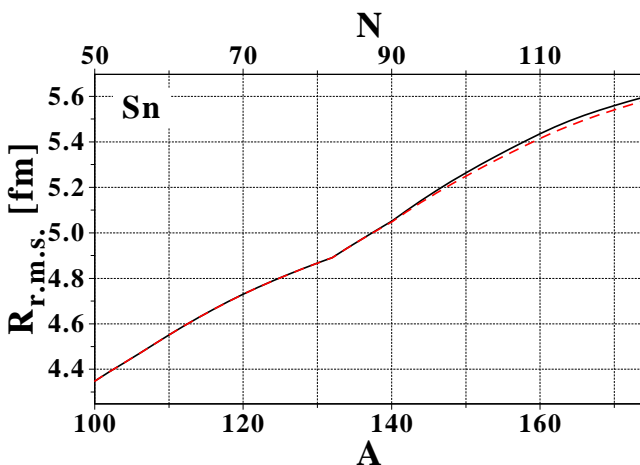


Figure 27: Same as FIG. 22 for Sn isotopes.

^{132}Sn				
N_{halo}	$0.13.10^{-2}$			
	e_i (MeV)	v_i^2	$N_{halo,i}$	P_i
$1i_{13/2}$	+2.648	0.000	0.000	0.0%
$3p_{1/2}$	+2.489	0.000	0.000	0.0%
$2f_{5/2}$	+1.661	0.000	0.000	0.0%
$3p_{3/2}$	+1.240	0.000	0.000	0.0%
$1h_{9/2}$	+1.141	0.000	0.000	0.0%
$2f_{7/2}$	-1.785	0.000	0.000	0.0%
<i>Other</i>	< -7.0	—	$\sim 0.13.10^{-2}$	—
^{146}Sn				
N_{halo}	$0.71.10^{-1}$			
	e_i (MeV)	v_i^2	$N_{halo,i}$	P_i
$1i_{13/2}$	+1.435	0.064	0.000	0.2%
$2f_{5/2}$	-0.056	0.155	0.004	2.4%
$3p_{1/2}$	-0.202	0.143	0.005	3.8%
$1h_{9/2}$	-0.401	0.262	0.001	0.3%
$3p_{3/2}$	-1.050	0.442	0.040	9.0%
$2f_{7/2}$	-3.037	0.923	0.017	1.9%
<i>Other</i>	< -7.0	—	$\sim 3.1.10^{-3}$	—
^{164}Sn				
N_{halo}	0.179			
	e_i (MeV)	v_i^2	$N_{halo,i}$	P_i
$1i_{13/2}$	-0.216	0.349	0.002	0.5%
$3p_{1/2}$	-1.347	0.804	0.052	6.6%
$2f_{5/2}$	-1.481	0.155	0.032	4.0%
$3p_{3/2}$	-2.143	0.923	0.072	7.8%
$1h_{9/2}$	-2.503	0.894	0.003	0.4%
$2f_{7/2}$	-4.301	0.975	0.014	1.4%
<i>Other</i>	< -7.0	—	$\sim 4.7.10^{-3}$	—
^{174}Sn				
N_{halo}	0.149			
	e_i (MeV)	v_i^2	$N_{halo,i}$	P_i
$1i_{13/2}$	-1.208	0.872	0.005	0.5%
$3p_{1/2}$	-1.854	0.979	0.049	5.0%
$2f_{5/2}$	-2.227	0.977	0.028	2.9%
$3p_{3/2}$	-2.665	0.989	0.054	5.5%
$1h_{9/2}$	-3.823	0.989	0.002	0.2%
$2f_{7/2}$	-5.014	0.996	0.009	0.9%
<i>Other</i>	< -7.0	—	$\sim 2.3.10^{-3}$	—

Table V: Same as TAB. III for Sn isotopes.

effect is seen in tin isotopes, and no significant halo formation is envisioned. We may add that the number of nucleons in the potential halo region is of the same order of magnitude as what one finds for a non-halo one-neutron p wave system such as ${}^{13}\text{Ne}$, where 0.12 neutron out of 6 reside in average in the classically forbidden region [120].

V. CONCLUSION

The existence of haloes at the neutron drip-line of medium-mass nuclei is still an open question. Several attempts to characterize their appearance have already been made using self-consistent mean-field relativistic or non-relativistic methods [78, 79, 80]. As a matter of fact, it was found that giant haloes constituted of 6 to 8 neutrons could emerge [77, 81, 82, 83, 84, 85]. However, those analysis were only based on basic observables such as the root-mean-square radius. Giant haloes were characterized by summing up occupations of loosely bound orbitals corresponding to nucleons which are part of the time well within the nuclear volume.

In the present work, a quantitative analysis method is developed to characterize haloes in a completely model-independent fashion. It is based on the decomposition of the intrinsic one-body density in terms of overlap functions. The definition of the halo, as the region where nucleons are spatially decorrelated from the others, was translated into specific features of the intrinsic one-body density, and of the energy spectrum of the $(N - 1)$ -body system. Properties of the excitation energy spectrum of the $(N - 1)$ -body system are translated into the existence of more or less sharp crossings between the individual components of the intrinsic density. We have highlighted the possibility of describing the halo in terms of three energy scales : the nucleon separation energy E , the energy spread ΔE of the bunch of low-lying states and the excitation energy E' of the remaining core with respect to the latter.

The region where the halo density dominates has been defined and validated by simulations. The definition does not rely on an *a priori* separation of the density into core and halo components. It is extracted from the analysis, using the total matter density as the only input. Several quantitative observables were defined : the average number of nucleons in the halo region, the influence of the halo region on the total nuclear extension, as well as the contributions from individual states to the total halo.

The new method was applied to HFB results from the spherical code HFBRAD, for chromium and tin isotopes. Cr isotopes appear to be ideal candidates for halo nuclei, and tin isotopes are usual milestones of mean-field-based methods.

For Cr isotopes, a significant number of nucleons is found in the halo region, and the absolute values are compliant with the ones found for light halo systems. The halo region is also found to influence significantly the nuclear extension. Multiple contributions from several states, including $l = 2$ ones, are deduced, which is not expected in the classical picture of few-body models. The notion of collective haloes in medium-mass nuclei is introduced. Such structures possess the same characteristics as the original haloes, but are formed by an admixture of states. The absolute number of nucleons in this

collective halo is of the order of ~ 0.5 nucleons, which is far less than in the giant halo picture. In our opinion this is much more realistic, as the enhancement of collectivity for medium-mass nuclei clearly prevents the formation of such a decorrelated 6 – 8 nucleons collective structure.

In the case of Sn isotopes, a very small contribution is found from the outer region, both in terms of the nucleon number and of the influence on the nuclear extension. For those reasons, the drip-line phenomenon discussed previously for tin isotopes [79] is rather a pronounced neutron skin effect. Such skin effects are also very interesting, as they emphasize the isovector dependence of the energy density functionals. Halo systems have on the other hand pronounced low density effects. The information gathered from both neutron skin and neutron halo nuclei are therefore complementary. We intend here to separate clearly such phenomena.

This preliminary study on two isotopic series gives very promising results and validates the theoretical grounds of the analysis. With upcoming new radioactive beam facilities, interaction cross sections are expected to be measurable in the drip-line region of $Z \approx 26$ elements. This would constitute a giant leap towards an extensive comparison between theoretical and experimental works on drip-line physics.

The second part of the present work [55] will be to use the tools introduced here for systematic studies over all predicted spherical nuclei, as well as for a quantitative analysis of the influence of pairing strength, regularization, density dependence on the halo phenomenon in medium-mass nuclei. In particular, we intend to address whether halo systems are affected by specific features of the pairing functional, like its range and locality.

Acknowledgments

We want to thank K. Bennaceur his support on HFBRAD, and F.M. Nunes for useful discussions on light halo nuclei. The proofreading of the manuscript by K. Bennaceur, J.-F. Berger, D. Lacroix and H. Goutte is greatly acknowledged. This work was supported by the U.S. National Science Foundation under Grant No. PHY-0456903.

Appendix A: PROPERTIES OF THE ONE-BODY DENSITY

1. Intrinsic wave functions

The exact Hamiltonian from Eq. 24 is invariant under translation and can be decomposed into a center-of-mass

$H_{c.m.}^N$ and an intrinsic part H_{intr}^N :

$$\left\{ \begin{array}{l} H_{c.m.}^N = -\frac{\hbar^2}{2mN} \left(\sum_{i=1}^N \nabla_i \right)^2 \\ H_{intr}^N = \sum_{\substack{i,j=1 \\ i < j}}^N \left[-\frac{\hbar^2}{2m^*} (\nabla_i - \nabla_j)^2 + V(r_{ij}) \right]. \end{array} \right. \quad (\text{A1})$$

This allows the factorization of $\Psi_{i,\vec{K}}^N(\vec{r}_1 \dots \vec{r}_N)$ into :

$$\Psi_{i,\vec{K}}^N(\vec{r}_1 \dots \vec{r}_N) = e^{i \vec{K} \cdot \vec{R}_N} \Phi_i^N(\vec{r}_1 \dots \vec{r}_N). \quad (\text{A2})$$

The intrinsic wave function Φ_i^N may be expressed using the $(N-1)$ independent Jacobi coordinates :

$$\vec{\xi}_i = \vec{r}_{i+1} - \frac{1}{i} \sum_{j=1}^i \vec{r}_j, \quad (\text{A3})$$

which are invariant under translation. Thus $\Phi_i^N(\vec{r}_1 \dots \vec{r}_N) \equiv \tilde{\Phi}_i^N(\vec{\xi}_1 \dots \vec{\xi}_{N-1})$ behaves for any vector \vec{a} as :

$$\Phi_i^N(\vec{r}_1 + \vec{a} \dots \vec{r}_N + \vec{a}) = \Phi_i^N(\vec{r}_1 \dots \vec{r}_N). \quad (\text{A4})$$

Orthogonality and completeness relationships of the set $\{\Phi_i^N\}$ are obtained in the sense of [104] :

$$\int d\vec{r}_1 \dots d\vec{r}_N \Phi_i^{N*}(\vec{r}_1 \dots \vec{r}_N) \delta(\vec{R}_N) \Phi_j^N(\vec{r}_1 \dots \vec{r}_N) = \delta_{ij}, \quad (\text{A5})$$

and

$$\begin{aligned} \sum_{i=1}^{+\infty} \Phi_i^{N*}(\vec{r}_1 \dots \vec{r}_N) \Phi_i^N(\vec{r}'_1 \dots \vec{r}'_N) \\ = \int d\vec{r} \frac{1}{A!} \det_{i,j=1..N} [\delta(\vec{r}_i - \vec{r}'_j + \vec{r})], \end{aligned} \quad (\text{A6})$$

where the extra integral over \vec{r} expresses the equivalence of translated configurations.

2. Decomposition of the N-body wave function

The ground state intrinsic wave function Φ_0^N can be expanded in terms of the complete orthonormal set of intrinsic $(N-1)$ -body wave functions Φ_ν^{N-1} , which are eigenstates of the $(N-1)$ -body intrinsic Hamiltonian [104, 105, 106, 107], such that^{(22),(23)} :

$$\begin{aligned} \Phi_0^N(\vec{r}_1 \dots \vec{r}_N) = \frac{1}{\sqrt{N}} \sum_\nu \Phi_\nu^{N-1}(\vec{r}_1 \dots \vec{r}_{N-1}) \\ \times \varphi_\nu(\vec{r}_N - \vec{R}_{N-1}). \end{aligned} \quad (\text{A7})$$

The states Φ_ν^{N-1} are ordered by increasing intrinsic energy, $\nu = 0$ corresponding to the ground state of the $(N-1)$ -body system. The overlap functions [121] $\varphi_\nu(\vec{r})$ represent the probability amplitudes to find a particle at position \vec{r} with respect to the center-of-mass of the $(N-1)$ -body system in the intrinsic state Φ_ν^{N-1} , if the initial system is in its ground state with zero momentum :

$$\begin{aligned} \varphi_\nu(\vec{r}) = \sqrt{N} \int d\vec{r}_1 \dots \vec{r}_{N-1} \Phi_\nu^{N-1*}(\vec{r}_1 \dots \vec{r}_{N-1}) \\ \times \delta(\vec{R}_{N-1}) \Phi_0^N(\vec{r}_1 \dots \vec{r}_{N-1}, \vec{r}). \end{aligned} \quad (\text{A8})$$

The latter quantity is of direct relevance for knockout reactions [108, 109, 122]. The spectroscopic amplitudes φ_ν are not the canonical overlaps of the N -body system defined in the laboratory frame. Indeed, they relate to the center-of-mass of the $(N-1)$ -body system fixed at the origin. The normalization of the overlap functions are the so-called spectroscopic factors [108, 109] :

$$S_\nu = \int d\vec{r} |\varphi_\nu(\vec{r})|^2. \quad (\text{A9})$$

3. Asymptotics of the overlap functions

The asymptotic properties of overlap functions are important, as the intrinsic one-body density is completely determined by those. The asymptotic equation satisfied by φ_ν is obtained from a further decomposition of the

²² The sum over ν in Eq. A7 corresponds to a discrete sum over the bound states of the $(N-1)$ -body system and an integral over the unbound resonant scattering channels.

²³ Antisymmetry is properly handled in Eq. A7, but the antisymmetrization is hidden in the overlap functions φ_ν . It is carried out in the same way as when a (antisymmetrized) Slater determinant is expanded according to its first column. In that case, one has :

$$\det_{i,j=1..N} [\varphi_i(\vec{r}_j)] = \sum_{k=1}^N (-1)^{k+1} \varphi_k(\vec{r}_1) \det_{\substack{i,j=1..N \\ i \neq k, j \neq 1}} [\varphi_i(\vec{r}_j)].$$

In the latter sum, each of the individual terms are not antisymmetric under the exchange of particle coordinates but the total sum is. For a more complete discussion on this subject we refer the reader to REF. [107].

intrinsic N -body Hamiltonian into :

$$H_{intr}^N = H_{intr}^{N-1} - \frac{\hbar^2(N-1)}{2mN} \left(\nabla_N - \frac{1}{N-1} \sum_{i=1}^{N-1} \nabla_i \right)^2 + \sum_{i=1}^N V(r_{iN}). \quad (\text{A10})$$

The trivial identity :

$$\int d\vec{r}_1 \dots d\vec{r}_{N-1} \Phi_\nu^{N-1*}(\vec{r}_1 \dots \vec{r}_{N-1}) \times \delta(\vec{R}_{N-1}) [H_{intr}^N - E_0^N] \Phi_0^N(\vec{r}_1 \dots \vec{r}_N) = 0 \quad (\text{A11})$$

gives a system of coupled channel equations for the overlap functions :

$$-\frac{\hbar^2}{2m \left(\frac{N-1}{N}\right)} \Delta_N \varphi_\nu(\vec{r}_N) - (E_0^N - E_\nu^{N-1}) \varphi_\nu(\vec{r}_N) + (N-1)\sqrt{N} \int d\vec{r}_1 \dots d\vec{r}_{N-1} \Phi_\nu^{N-1*}(\vec{r}_1 \dots \vec{r}_{N-1}) \times \delta(\vec{R}_{N-1}) V(|\vec{r}_N - \vec{r}_{N-1}|) \Phi_0^N(\vec{r}_1 \dots \vec{r}_N) = 0. \quad (\text{A12})$$

The kinetic term appears with a reduced mass $m^* = \frac{N-1}{N}m$ corresponding to the effective mass of a particle with respect to the center-of-mass of the $(N-1)$ others. For large distances $|\vec{r}_N - \vec{R}_{N-1}| > R$, the nuclear interaction vanishes and the radial part $\bar{\varphi}_\nu$ of the overlap functions become solutions of the free Schrödinger equation :

$$\left[\left(\frac{d^2}{dr^2} + \frac{2}{r} \frac{d}{dr} - \frac{l_\nu(l_\nu + 1)}{r^2} \right) - \kappa_\nu^2 \right] \bar{\varphi}_\nu^\infty(r) = 0, \quad (\text{A13})$$

with $\kappa_\nu = \sqrt{-\frac{2m^*\epsilon_\nu}{\hbar^2}}$, where $\epsilon_\nu = (E_0^N - E_\nu^{N-1})$ is minus the nucleon separation energy to reach Φ_ν^{N-1} . Solutions of the asymptotic free Schrödinger equation take the form :

$$\varphi_\nu^\infty(\vec{r}) = \sqrt{B_\nu} h_{l_\nu}(i\kappa_\nu r) Y_{l_\nu}^{m_\nu}(\theta, \varphi). \quad (\text{A14})$$

4. Intrinsic density

In the laboratory frame, the one-body density is the expectation value of the operator :

$$\hat{\rho}(\vec{r}) = \sum_{i=1}^N \delta(\vec{r} - \hat{\vec{r}}_i), \quad (\text{A15})$$

which leads for the N -body ground state to :

$$\begin{aligned} \rho(\vec{r}) &= N \int d\vec{r}_1 \dots d\vec{r}_{N-1} |\Psi_0^N(\vec{r}_1 \dots \vec{r}_{N-1}, \vec{r})|^2 \\ &= N \int d\vec{\xi}_1 \dots d\vec{\xi}_{N-2} d\vec{R}_{N-1} \\ &\quad \times |\tilde{\Phi}_0^N(\vec{\xi}_1 \dots \vec{\xi}_{N-2}, \vec{r} - \vec{R}_{N-1})|^2. \end{aligned} \quad (\text{A16})$$

Using Eq. A4, one easily proves that the one-body density in the laboratory frame is translationally invariant $\rho(\vec{r} + \vec{a}) = \rho(\vec{r})$, and thus is uniform. This is a general property of translationally invariant systems which underlines that the density in the laboratory frame is not the proper tool to study self-bound systems.

The relevant object for self-bound systems is the intrinsic one-body density matrix, defined as the expectation value of the operator :

$$\begin{aligned} \hat{\rho}_{[1]}(\vec{r}, \vec{r}') &= \delta(\vec{R}_N) \sum_{i=1}^N \delta(\vec{r} - \hat{\vec{r}}_i + \hat{\vec{R}}_{N-1}^i) \\ &\quad \times \delta(\vec{R}'_N) \sum_{j=1}^N \delta(\vec{r}' - \hat{\vec{r}}'_j + \hat{\vec{R}}'_{N-1}^j) \\ &\quad \times \prod_{\substack{k,l=1..N \\ k,l \neq i,j}} \delta(\hat{\vec{r}}_k - \hat{\vec{r}}_l), \end{aligned} \quad (\text{A17})$$

where :

$$\hat{\vec{R}}_{N-1}^i = \frac{1}{N-1} \sum_{\substack{j=1 \\ j \neq i}}^N \hat{\vec{r}}_j. \quad (\text{A18})$$

This is one of two possible definitions for the intrinsic one-body density, depending on the pivot point used as reference for the transformed coordinate system (with reference to the center-of-mass of the N -body system, or the center-of-mass of the remaining $(N-1)$ -body one). Using Eqs. A5 and A7, one obtains [106, 110, 111] :

$$\begin{aligned} \rho_{[1]}(\vec{r}, \vec{r}') &= N \int d\vec{r}_1 \dots d\vec{r}_{N-1} \Phi_0^{N*}(\vec{r}_1 \dots \vec{r}_{N-1}, \vec{r}') \\ &\quad \times \delta(\vec{R}_{N-1}) \Phi_0^N(\vec{r}_1 \dots \vec{r}_{N-1}, \vec{r}) \\ &= \sum_\nu \varphi_\nu^*(\vec{r}') \varphi_\nu(\vec{r}), \end{aligned} \quad (\text{A19})$$

which shows that the intrinsic one-body density matrix is completely determined by the overlap functions [110].

The intrinsic one-body density $\rho_{[1]}(\vec{r})$ is the local part of the intrinsic density matrix, and is the expectation value of the operator :

$$\hat{\rho}_{[1]}(\vec{r}) = \delta(\vec{R}_N) \sum_{i=1}^N \delta(\vec{r} - \hat{\vec{r}}_i + \hat{\vec{R}}_{N-1}^i). \quad (\text{A20})$$

According to Eq. A19, one has :

$$\rho_{[1]}(\vec{r}) = \sum_\nu |\varphi_\nu(\vec{r})|^2 = \sum_\nu \frac{2l_\nu + 1}{4\pi} |\bar{\varphi}_\nu(r)|^2. \quad (\text{A21})$$

Appendix B: DETERMINATION OF THE HALO REGION

Let us start from a very crude toy model, where everything is analytical. The total density ρ is assumed to

be a superposition of a core ρ_c and a tail ρ_h , both taking the form :

$$\rho_i(r) = A_i \kappa_i e^{-\kappa_i r}. \quad (\text{B1})$$

This amounts to considering that the asymptotic regime is reached in the region of the crossing between ρ_c and ρ_h , and we neglect for now the $1/r^2$ factor. In this model the second-order log-derivative of the total density is analytical, as well as the exact positions of (i) its maximum r_{max} (ii) the point r_{10} where the halo density is exactly equal to ten times the core one. Then, the ratio $\mathcal{R}(r_{10}) = \log''\rho(r_{10})/\log''\rho(r_{max})$ can be evaluated and becomes in the limit of interest $\frac{\kappa_h}{\kappa_c} \rightarrow 0$:

$$\mathcal{R}(r_{10}) \xrightarrow{\frac{\kappa_h}{\kappa_c} \rightarrow 0} \frac{40}{121} + \mathcal{O}\left[\left(\frac{\kappa_h}{\kappa_c}\right)^2\right]. \quad (\text{B2})$$

This shows that the position where there is a fixed ratio of 10 between ρ_c and ρ_h is equivalently obtained by finding the position where there is a given ratio between the value of the second-order log-derivative of the density and its maximal value. The critical value of $40/121 \approx 0.33$ found in the toy model is not believed to be accurate for complex nuclei, as (i) the asymptotic regime is not reached at the crossing point, and is more complicated because of the $1/r^2$ factor (ii) the total density is a superposition of more than two components. However, we expect the one-to-one correspondence between ratios on the densities and ratios on $\log''\rho$ to hold in realistic cases. Thus, *the position where the halo dominates the core by one order of magnitude can be found using $\log''\rho$ as the only input*.

More realistic model calculations have been used to characterize the position of r_0 . The total density is taken as a linear combination of core and halo contributions. Their relative normalizations are free parameters in this simulation, allowing to artificially change the fraction of halo in the total density :

$$\rho_{tot}(r) = N_C \rho_c(r) + \sum_{\nu=1}^m N_\nu \rho_\nu(r), \quad (\text{B3})$$

where N_C and $N_H = \sum_{\nu=1}^m N_\nu$ are the number of nucleons in the core part and in the halo part, respectively. The densities ρ_c and ρ_ν are normalized to 1. We considered (i) simple models, where the core and each halo components are defined as :

$$\begin{cases} \rho_i(r) = \frac{1}{\mathcal{N}_i} & r < R_0, \\ \rho_i(r) = \frac{1}{\mathcal{N}_i} e^{\frac{R_0-r}{a_i}} & r > R_0, \end{cases} \quad (\text{B4})$$

\mathcal{N}_i standing for a normalization constant. This model only accounts for the basic features of the nuclear density : a uniform core of radius R_0 and a spatial extension becoming larger as $a_i \rightarrow 0$ (ii) double Fermi models,

where the un-physical sharp edge in the logarithmic representation of the previous density is smoothed out :

$$\rho_i(r) = \frac{\rho_0}{1 + e^{\frac{r-R_0}{a_i}}} \quad (\text{B5})$$

(iii) semi-phenomenological models, which fulfill the asymptotic behavior of Eq. 36. Core and tail densities vanish at $r = 0$, as well as their derivatives with respect to x, y and z , in order to avoid singularities at the nucleus center [123]. In REFS. [124, 125, 126], such densities were adjusted on experimental data. The core part was defined as :

$$\rho_c(r) = \frac{\rho_{0,c}}{1 + \left[\frac{1 + \left(\frac{r}{R_{0,c}} \right)^2}{2} \right]^\alpha \left[e^{\frac{r-R_{0,c}}{a_c}} + e^{\frac{-r-R_{0,c}}{a_c}} \right]}, \quad (\text{B6})$$

where $\alpha = 1$ for neutrons, and the halo density as :

$$\rho_h(r) = \rho_{0,t} \left[\frac{r^2}{(r^2 + R_{0,t}^2)} \right] e^{-\frac{r}{a_t}} \quad (\text{B7})$$

(iv) more realistic models, where the core density is still defined as in Eq. B6, but the halo contributions are realistic wave functions obtained from self-consistent HFB calculations of Cr and Sn isotopes.

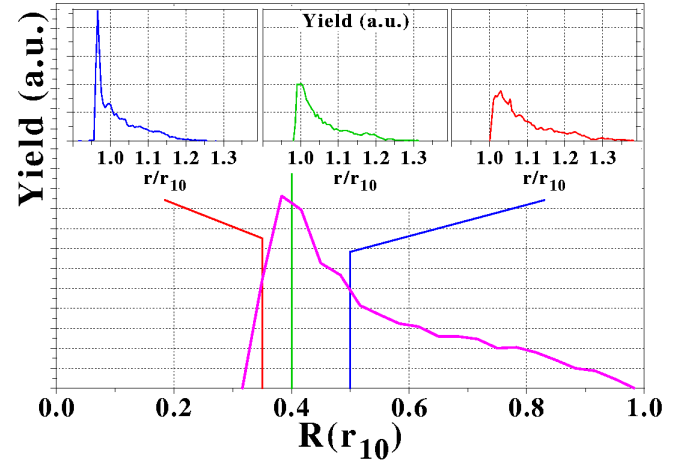


Figure 28: (Main panel) Ratio between the second-order log-density at r_{10} and its peak value $\log''\rho(r_{max})$ (Top panels) Ratio between r_1 where $\mathcal{R}(r)$ is equal to a fixed value (left panel : $\mathcal{R}(r) = 0.35$, middle panel : $\mathcal{R}(r) = 0.4$, right panel : $\mathcal{R}(r) = 0.5$), and r_{10} .

The results from a wide panel of test cases are presented in FIG. 28. In each of those cases, the exact position of r_{10} is computed, as well as the ratio $\mathcal{R}(r_{10})$ at this point. From the main panel of FIG. 28, the latter ratio is 0.4 in average, greater than in the toy model case for the reasons detailed above. The distribution of $\mathcal{R}(r_{10})$ is asymmetric, but the tail towards higher values

corresponds to extreme situations which will be taken into account through error bars.

The positions r where $\mathcal{R}(r)$ takes specific values are also evaluated. The associated distributions of r/r_{10} are displayed in the inserts in FIG. 28. For $\mathcal{R}(r) = 121/40$ (top-left panel), the resulting position r is in most cases below r_{10} . As a consequence, the average ratio between tail and core components in the density will be significantly below 10. On the contrary for $\mathcal{R}(r) = 1/2$ (top-right panel), r is significantly larger than r_{10} , and ρ_h/ρ_c will be over 10 in average. For those reasons, it appears that r_0 will be a good approximation of r_{10} when :

$$\mathcal{R}(r_0) = \frac{2}{5}. \quad (\text{B8})$$

Secondly, we account for the fact that a difference by one order of magnitude between core and halo densities is somewhat arbitrary and cannot be exactly achieved for all densities, by adding theoretical error bars to the definition of r_0 . We allow $\mathcal{R}(r_0)$ to vary between 0.35 and 0.50 to account for the uncertainties previously detailed. The upper margin is greater than the lower one because of the asymmetry of the peak in FIG. 28.

[1] P. G. Hansen and B. Jonson, *Europhys. Lett.* **4**, 409 (1987).

[2] I. Tanihata *et al.*, *Phys. Rev. Lett.* **55**, 2676 (1985).

[3] I. Tanihata *et al.*, *Phys. Lett.* **B160**, 380 (1985).

[4] M. V. Zhukov *et al.*, *Phys. Rep.* **231**, 151 (1993).

[5] I. Tanihata *et al.*, *Phys. Lett.* **B160**, 380 (1985).

[6] M. Fukuda *et al.*, *Phys. Lett.* **B268**, 339 (1991).

[7] M. Zahar *et al.*, *Phys. Rev.* **C48**, R1484 (1993).

[8] I. J. Thompson and M. V. Zhukov, *Phys. Rev.* **C53**, 708 (1996).

[9] D. Bazin *et al.*, *Phys. Rev. Lett.* **74**, 3569 (1995).

[10] R. Kanungo, I. Tanihata, Y. Ogawa, H. Toki, and A. Ozawa, *Nucl. Phys.* **A701**, 378 (2002).

[11] M. V. Zhukov and I. J. Thompson, *Phys. Rev.* **C52**, 3505 (1995).

[12] T. Minamisono *et al.*, *Phys. Rev. Lett.* **69**, 2058 (1992).

[13] W. Schwab *et al.*, *Z. Phys.* **A350**, 283 (1995).

[14] R. E. Warner *et al.*, *Phys. Rev.* **C52**, R1166 (1995).

[15] F. Negoita *et al.*, *Phys. Rev.* **C54**, 1787 (1996).

[16] R. Kanungo *et al.*, *Phys. Lett.* **B571**, 21 (2003).

[17] H. Jeppesen *et al.*, *Nucl. Phys.* **A739**, 57 (2004).

[18] R. Morlock *et al.*, *Phys. Rev. Lett.* **79**, 3837 (1997).

[19] Z. Ren, A. Faessler, and A. Bobyk, *Phys. Rev.* **C57**, 2752 (1998).

[20] C. J. Lin, Z. H. Liu, H. Q. Z. Y. W. Wu, F. Yang, and M. Ruan, *Chin. Phys. Lett.* **18**, 1183 (2001).

[21] Z. H. Liu *et al.*, *Phys. Rev.* **C64**, 034312 (2001).

[22] J. G. Chen *et al.*, *Eur. Phys. J.* **A23**, 11 (2005).

[23] D. V. Fedorov, A. S. Jensen, and K. Riisager, *Phys. Rev.* **C50**, 2372 (1994).

[24] F. Nunes, I. J. Thompson, and R. C. Johnson, *Nucl. Phys.* **A609**, 43 (1996).

[25] F. Nunes, J. A. Christley, I. J. Thompson, R. C. Johnson, and V. D. Efros, *Nucl. Phys.* **A596**, 171 (1996).

[26] J. M. Bang, *Phys. Rep.* **264**, 27 (1996).

[27] K. Riisager, D. V. Fedorov, and A. S. Jensen, *Europhys. Lett.* **49**, 547 (2000).

[28] A. S. Jensen and M. V. Zhukov, *Nucl. Phys.* **A693**, 411 (2001).

[29] D. V. Fedorov, A. S. Jensen, and K. Riisager, *Phys. Lett.* **B312**, 1 (1993).

[30] A. S. Jensen and K. Riisager, *Phys. Lett.* **B480**, 39 (2000).

[31] D. V. Fedorov, A. S. Jensen, and K. Riisager, *Phys. Rev.* **C49**, 201 (1994).

[32] P. Hohenberg and W. Kohn, *Phys. Rev.* **136**, B864 (1964).

[33] W. Kohn and L. Sham, *Phys. Rev.* **140**, A1133 (1965).

[34] R. Fukuda, T. Kotani, Y. Suzuki, and S. Yokojima, *Prog. Theor. Phys.* **92**, 833 (1994).

[35] P. Ring and P. Schuck, *The Nuclear Many-Body Problem* (Springer-Verlag, New-York, 1980).

[36] M. Bender, P.-H. Heenen, and P.-G. Reinhard, *Rev. Mod. Phys.* **75**, 121 (2003).

[37] T. H. Skyrme, *Phil. Mag.* **1**, 1043 (1956).

[38] D. Vautherin and D. M. Brink, *Phys. Rev.* **C5**, 626 (1972).

[39] J. Dechargé and D. Gogny, *Phys. Rev.* **C21**, 1568 (1980).

[40] A. Bouyssy, J.-F. Mathiot, N. V. Giai, and S. Marcos, *Phys. Rev.* **C36**, 380 (1987).

[41] P.-G. Reinhard, *Rep. Prog. Phys.* **52**, 439 (1989).

[42] Y. K. Gambhir, P. Ring, and A. Thimet, *Ann. Phys.* **198**, 132 (1990).

[43] P. Ring, *Prog. Part. Nucl. Phys.* **37**, 193 (1993).

[44] B. G. Todd and J. Piekarewicz, *Phys. Rev.* **C67**, 044317 (2003).

[45] R. J. Furnstahl, *J. Phys.* **G31**, S1357 (2005).

[46] T. Duguet, K. Bennaceur, T. Lesinski, and J. Meyer, *nucl-th/0606037*.

[47] M. Samyn, S. Goriely, P.-H. Heenen, J. M. Pearson, and J. F. Tondeur, *Nucl. Phys.* **A700**, 142 (2002).

[48] S. Goriely, M. Samyn, P.-H. Heene, J. M. Pearson, and F. Tondeur, *Phys. Rev.* **C66**, 024326 (2002).

[49] S. Goriely, M. Samyn, M. Bender, and J. M. Pearson, *Phys. Rev.* **C68**, 054325 (2003).

[50] M. Samyn, S. Goriely, M. Bender, and J. M. Pearson, *Phys. Rev.* **C70**, 044309 (2004).

[51] J. Dobaczewski and W. Nazarewicz, *Prog. Theor. Phys. Suppl.* **146**, 70 (2002).

[52] M. Bender and P.-H. Heenen, *Nucl. Phys.* **A713**, 390 (2003).

[53] T. Duguet, M. Bender, P. Bonche, and P.-H. Heenen, *Phys. Lett.* **B559**, 201 (2004).

[54] J. L. Egido and L. M. Robledo, *Lect. Notes Phys.* **641**, 269 (2004).

[55] V. Rotival, K. Bennaceur, and T. Duguet, In preparation.

[56] K. Riisager, A. S. Jensen, and P. Møller, Nucl. Phys. **A548**, 393 (1992).

[57] T. Mizu, W. Nazarewicz, and S. Åberg, Nucl. Phys. **A614**, 44 (1997).

[58] T. H. Koopmans, Physica **1**, 104 (1934).

[59] S. B. Khadkikar and V. B. Kamble, Nucl. Phys. **A225**, 352 (1974).

[60] L. Jacqua, M. A. Hæsan, J. P. Vary, and B. R. Barrett, Phys. Rev. **C46**, 2333 (1992).

[61] R. Roth *et al.*, Phys. Rev. **C73**, 044312 (2006).

[62] J. Dobaczewski, H. Flocard, and J. Treiner, Nucl. Phys. **A422**, 103 (1984).

[63] J. Dobaczewski *et al.*, Phys. Rev. **C53**, 2809 (1996).

[64] J. Terasaki, P.-H. Heenen, H. Flocard, and P. Bonche, Nucl. Phys. **A600**, 371 (1996).

[65] H. Toki, Y. Sugahara, D. Hirata, B. V. Carlson, and I. Tanihata, Nucl. Phys. **A524**, 633 (1991).

[66] M. M. Sharma, M. A. Nagajaran, and P. Ring, Phys. Lett. **B312**, 377 (1993).

[67] Y. Sugahara and H. Toki, Nucl. Phys. **A579**, 557 (1994).

[68] N. N. Bogolyubov, Sov. Phys. JETP **7**, 41 (1958).

[69] N. N. Bogolyubov, Sov. Phys. Usp. **2**, 236 (1959).

[70] N. N. Bogolyubov and V. G. Soloviev, Sov. Phys. Doklady **4**, 143 (1959).

[71] N. Tajima, H. Flocard, P. Bonche, J. Dobaczewski, and P.-H. Heenen, Nucl. Phys. **A542**, 355 (1992).

[72] K. Bennaceur, J. Dobaczewski, and M. Ploszajczak, Phys. Rev. **C60**, 034308 (1999).

[73] K. Bennaceur, J. Dobaczewski, and M. Ploszajczak, Phys. Lett. **B496**, 154 (2000).

[74] I. Hamamoto and B. Mottelson, Phys. Rev. **C68**, 034312 (2003).

[75] I. Hamamoto, Phys. Rev. **C69**, 064302 (2004).

[76] I. Hamamoto, Phys. Rev. **C71**, 037302 (2005).

[77] J. Meng and P. Ring, Phys. Rev. Lett. **80**, 460 (1998).

[78] B. Nerlo-Pomorska, K. Pomorski, J.-F. Berger, and J. Dechargé, Eur. Phys. J. **A8**, 19 (2000).

[79] S. Mizutori, J. Dobaczewski, G. A. Lalazissis, W. Nazarewicz, and P.-G. Reinhard, Phys. Rev. **C61**, 044326 (2000).

[80] S. Im and J. Meng, Phys. Rev. **C61**, 047302 (2000).

[81] N. Sandulescu, L. S. Geng, H. Toki, and G. Hillhouse, Phys. Rev. **C68**, 054323 (2003).

[82] L. S. Geng, H. Toki, and J. Meng, Mod. Phys. Lett. **A19**, 2171 (2004).

[83] M. Kaushik, D. Singh, and H. L. Yadav, Acta Phys. Slov. **55**, 181 (2005).

[84] M. Grasso, S. Yoshida, N. Sandulescu, and N. V. Giai, Phys. Rev. **C74**, 064317 (2006).

[85] J. Terasaki, S. Q. Zhang, S. G. Zhou, and J. Meng, Phys. Rev. **C74**, 054318 (2006).

[86] K. Bennaceur and J. Dobaczewski, Comp. Phys. Comm. **168**, 96 (2005).

[87] E. Chabanat, P. Bonche, P. Haensel, J. Meyer, and R. Schaeffer, Nucl. Phys. **A627**, 710 (1997).

[88] E. Chabanat, P. Bonche, P. Haensel, J. Meyer, and R. Schaeffer, Nucl. Phys. **A635**, 231 (1998).

[89] F. Tondeur, Nucl. Phys. **A315**, 353 (1979).

[90] S. J. Krieger, P. Bonche, H. Flocard, P. Quentin, and M. S. Weiss, Nucl. Phys. **A517**, 275 (1990).

[91] G. F. Bertsch and H. Esbensen, Ann. Phys. (NY) **209**, 327 (1991).

[92] N. Tajima, P. Bonche, H. Flocard, P.-H. Heenen, and M. S. Weiss, Nucl. Phys. **A551**, 434 (1993).

[93] J. Terasaki, P.-H. Heenen, P. Bonche, J. Dobaczewski, and H. Flocard, Nucl. Phys. **A593**, 1 (1995).

[94] D1S Interaction Results Database, <http://www-phynu.cea.fr/>.

[95] J. Dobaczewski, M. V. Stoitsov, and W. Nazarewicz, AIP Conf. Proc. **726**, 51 (2004).

[96] I. Angeli, Atomic Data and Nuclear Data Tables **87**, 185 (2004).

[97] G. Audi, A. H. Wapstra, and C. Thibault, Nucl. Phys. **A739**, 337 (2003).

[98] P. Lubiński *et al.*, Phys. Rev. **C57**, 2962 (1998).

[99] R. H. Helm, Phys. Rev. **104**, 1466 (1956).

[100] M. Rosen, R. Raphael, and H. Überall, Phys. Rev. **163**, 927 (1957).

[101] R. Raphael and M. Rosen, Phys. Rev. **C1**, 547 (1970).

[102] N. Tajima, Phys. Rev. **C69**, 034305 (2004).

[103] J. Friedrich and N. Voegler, Nucl. Phys. **A373**, 192 (1982).

[104] D. V. Neck, A. E. L. Dieperink, and M. Waroquier, Phys. Rev. **C53**, 2231 (1996).

[105] D. V. Neck, M. Waroquier, A. E. L. Dieperink, S. C. Pieper, and V. R. Pandharipande, Phys. Rev. **C57**, 2308 (1998).

[106] D. V. Neck and M. Waroquier, Phys. Rev. **C58**, 3359 (1998).

[107] J. Escher, B. K. Jennings, and H. S. Sherif, Phys. Rev. **C64**, 065801 (2001).

[108] C. F. Clement, Nucl. Phys. **A213**, 469 (1973).

[109] C. F. Clement, Nucl. Phys. **A213**, 493 (1973).

[110] D. V. Neck, M. Waroquier, and K. Heyde, Phys. Lett. **B314**, 255 (1993).

[111] A. V. Shebeko, P. Papakonstantinou, and E. Mavromatis, Eur. Phys. J. **A27**, 143 (2006).

[112] M. Levy, J. P. Perdew, and V. Sahni, Phys. Rev. **A30**, 2745 (1984).

[113] R. M. Dreizler and E. K. U. Gross, *Density Functional Theory* (Springer, Berlin, 1990).

[114] T. Duguet, P. Bonche, P.-H. Heenen, and J. Meyer, Phys. Rev. **C65**, 014310 (2002).

[115] T. Duguet, P. Bonche, P.-H. Heenen, and J. Meyer, Phys. Rev. **C65**, 014311 (2002).

[116] D. V. Neck, physics/0609037.

[117] C. A. Bertulani, H.-W. Hammer, and U. V. Kolck, Nucl. Phys. **A712**, 37 (2002).

[118] M. Abramowitz and I. Stegun, *Handbook of Mathematical Functions* (Dover, New York, 1965).

[119] G. Dahlquist and Å. Björck, *Numerical Methods* (Prentice-Hall, Englewood Cliffs, NJ, 1974).

[120] F. Nunes, Priv. comm.

[121] J. M. Bang, F. G. Gareev, W. T. Pinkston, and J. S. Vaagen, Phys. Rep. **125**, 253 (1985).

[122] A. E. L. Dieperink and J. T. de Forest, Phys. Rev. **C10**, 543 (1974).

[123] D. Berdichevsky and U. Mosel, Nucl. Phys. **A388**, 205 (1982).

[124] Y. K. Gambhir and S. H. Patil, Z. Phys. **A321**, 161 (1985).

[125] Y. K. Gambhir and S. H. Patil, Z. Phys. **A324**, 9 (1986).

[126] A. Bhagwat, Y. K. Gambhir, and S. H. Patil, Eur. Phys. J. **A8**, 511 (2000).